Biophysical Journal
Article

Biophysical Society

# Vesicle Adhesion and Fusion Studied by Small-Angle X-Ray Scattering

Karlo Komorowski,[1,2] Annalena Salditt,[1] Yihui Xu,[1] Halenur Yavuz,[2] Martha Brennich,[3] Reinhard Jahn,[2] and Tim Salditt[1,*]

[1]Institut für Röntgenphysik, Georg-August-Universität Göttingen, Göttingen, Germany; [2]Department of Neurobiology, Max-Planck-Institute for Biophysical Chemistry, Göttingen, Germany; and [3]European Molecular Biology Laboratory, Grenoble Outstation, Grenoble, France

ABSTRACT We have studied the adhesion state (also denoted by docking state) of lipid vesicles as induced by the divalent ions $Ca^{2+}$ or $Mg^{2+}$ at well-controlled ion concentration, lipid composition, and charge density. The bilayer structure and the interbilayer distance in the docking state were analyzed by small-angle x-ray scattering. A strong adhesion state was observed for DOPC:DOPS vesicles, indicating like-charge attraction resulting from ion correlations. The observed interbilayer separations of ~1.6 nm agree quantitatively with the predictions of electrostatics in the strong coupling regime. Although this phenomenon was observed when mixing anionic and zwitterionic (or neutral) lipids, pure anionic membranes (DOPS) with highest charge density $\sigma$ resulted in a direct phase transition to a multilamellar state, which must be accompanied by rupture and fusion of vesicles. To extend the structural assay toward protein-controlled docking and fusion, we have characterized reconstituted *N*-ethylmaleimide-sensitive factor attachment protein receptors in controlled proteoliposome suspensions by small-angle x-ray scattering.

## INTRODUCTION

Membrane fusion is a ubiquitous physiological process on both the cellular and subcellular level. A well-known example is the fusion of neurotransmitter-filled synaptic vesicles with the presynaptic plasma membrane (1). The fusion and the subsequent release of neurotransmitters are essential for nerve conduction, which is mediated by proteins known as soluble *N*-ethylmaleimide-sensitive factor attachment protein receptors (SNAREs) (2). Neuronal SNAREs comprise both synaptobrevin 2 (Syb), situated in the membrane of the synaptic vesicle, as well as syntaxin 1a (Syx) and SNAP-25 (SN25), which in turn are anchored in the presynaptic plasma membrane. According to the zippering hypothesis, the N- to C-terminal assembly to a four-helix bundle, named the SNARE complex, provides the driving force to bring opposing membranes into close contact and therefore initiates the merger (2).

Despite significant experimental efforts, e.g., (3,4), many important details of the membrane fusion pathway, in particular concerning the intermediate structures of the membrane and the corresponding energy barriers, are still under debate. At the same time, numerical studies have provided interesting insight into possible structures and mechanisms (5,6), which in turn require experimental verification. From studies of multilamellar model membranes, we know that the planar bilayer topology becomes unstable upon dehydration, and stalks begin to form for certain lipids once a critical (minimal) water layer thickness $d_w$ is reached between opposing bilayers (7–11). A limitation of these experiments is the fact that the critical osmotic pressure is extremely high and cannot be reached in solution but requires partial hydration in vapor pressure chambers. Important biochemical and biophysical parameters such as ionic strength cannot be used in such a setup. It is therefore of interest to investigate the equilibrium spacing between adhering lipid vesicles in solution, especially in the presence of controlled concentrations of monovalent or divalent ions such as $Ca^{2+}$. In particular, it is important to see whether adhesion and eventually fusion can be induced by controlled variation of divalent ion concentration and to quantify the corresponding electrostatistical forces (12,13). Experimentally, adhesion and fusion can be studied both in protein-free vesicles induced by $Ca^{2+}$ as well as in vesicles with reconstituted SNAREs (also denoted as proteoliposomes) because reconstitution protocols are well established (3).

*Submitted August 24, 2017, and accepted for publication February 28, 2018.*

*Correspondence: tsaldit@gwdg.de

Editor: Georg Pabst.

https://doi.org/10.1016/j.bpj.2018.02.040

In this work, we use small-angle x-ray scattering (SAXS) as a well-established technique for structure analysis of lipid vesicles in solution (14–16) to characterize the adhesion (or docking) state of vesicles. To this end, we primarily address "physical" adhesion induced by $Ca^{2+}$ in pure lipid vesicles. We hence provide an experimental investigation of the contact zone, which has also received much attention in recent molecular dynamics (MD) simulations (17–19). Importantly, we find that the interbilayer distance in the strong adhesion state is governed by condensation of the divalent counterion according to the regime of strong coupling (13). In Outlook: SNARE-liposomes, we present SAXS experiments using vesicles with reconstituted SNAREs. For the latter, we use the mutant Syb$\Delta$84, which was shown to induce adhesion but not to promote full fusion (3). In this way, intermediate states of a SNARE-mediated liposome fusion pathway could be made accessible for SAXS. Note that the adhesion state of both protein-free vesicles and proteoliposomes, with two bilayers brought into close apposition, is likely to be governed by strong electrostatic and osmotic forces.

The main aim of this work is hence to probe the bilayer structure and the interbilayer water spacing $d_w$, with molecular resolution as quantified by the electron density profile (EDP) normal to the membranes. Following suitable preparation protocols of vesicles, the first challenge is the preparation and identification of the adhesion or docking state. As a long-term goal, we want to control and distinguish a nonreacted, a docked, and a fused state, as illustrated in Fig. 1.

We thus first address vesicle preparation, protein reconstitution, and SAXS analysis in the Materials and Methods following this introduction. Subsequently, results will be presented and discussed, first for noninteracting unilamellar lipid vesicles and then for the adhesion state of vesicles induced by $CaCl_2$ and $MgCl_2$. The interbilayer distances obtained from adhered vesicles will be discussed in terms of interaction potentials. The study will close with an outlook toward x-ray structural investigations of SNARE-mediated liposome docking and fusion and with a summary of the main findings. Auxiliary data sets and further evaluations as well as additional technical details are included as Supporting Material.

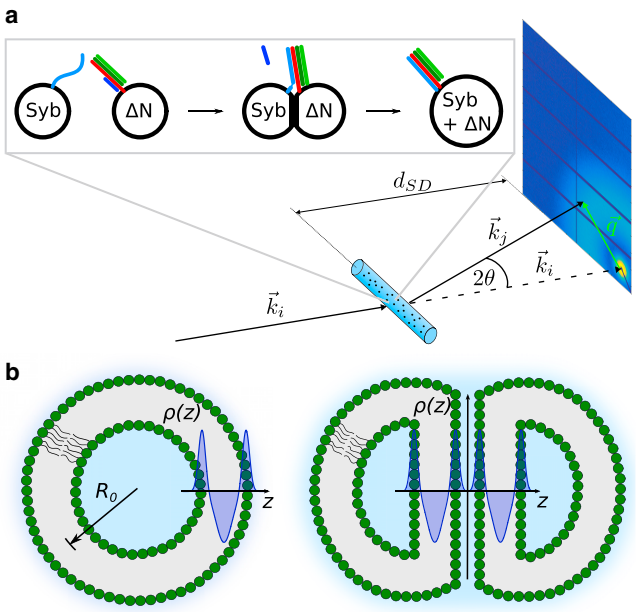


FIGURE 1 (*a*) SAXS geometry and isotropic two-dimensional diffraction pattern as measured by an area detector (here, scattering from DOPC:DOPE (1:1) vesicles). The distance between the sample plane and the detector is denoted by $d_{SD}$. The momentum transfer vector is given by $\vec{q} = \vec{k}_j - \vec{k}_i$, where $\vec{k}_i$ and $\vec{k}_j$ are the wave vectors of the incident and the scattered x-ray beam, respectively. (*b*) Sketch of a "free" vesicle with the radius $R_0$ (*left*) and of two docked vesicles with an extended interface between two opposing bilayers (*right*) is shown. For both illustrations, three Gaussians describing the EDP $\rho(z)$ of a bilayer are indicated (one Gaussian for each headgroup region and one Gaussian for the hydrophobic chain region). To see this figure in color, go online.

## MATERIALS AND METHODS

### Preparation of vesicles

The lipids dioleoylphosphatidylcholine (DOPC), dioleoylphosphatidylethanolamine (DOPE), dioleoylphosphatidylserine (DOPS), and cholesterol were purchased as lyophilized powders from Avanti Polar Lipids (Alabaster, AL). As a first step, the lipids were dissolved in chloroform and mixed at the desired molar ratio. Chloroform was then evaporated under a stream of nitrogen. The resulting dried lipid film was subsequently hydrated with ultrapure water (Milli-Q; Merck, Darmstadt, Germany) to a final lipid concentration of either 5 mg/mL for DOPC:DOPE:DOPS:Chol or 10 mg/mL for all other lipid mixtures. To achieve a homogeneous phase, the mixture was sonicated to clarity using a tip sonicator (SONOPULS HD 3100; Bandelin, Berlin, Germany) at amplitude 40% and pulse duration 0.5 s/0.5 s and at least five times for 60 s, with cooling periods on ice. After sonication, the vesicle suspension was stepwise extruded through polycarbonate membranes with pore sizes of 100, 50, and 30 nm in diameter (in that order, for each round 25 times) using a Mini-Extruder from Avanti Polar Lipids.

For the investigation of $CaCl_2$- and $MgCl_2$-induced vesicle adhesion, the DOPC:DOPS mixtures were hydrated with either ultrapure water or a 100 mM glucose solution to a final concentration of 10 mg/mL and subsequently vortexed. Afterwards, the vesicles were extruded through membranes of a pore size of 100 nm in diameter. $CaCl_2$ and $MgCl_2$, suspended either in ultrapure water or in a 100 mM glucose solution, were added to the vesicle suspension before the experiment.

Size distributions of the vesicles were quantified by dynamic light scattering (DLS), both for noninteracting vesicles (included as Fig. S1) and for the calcium-induced adhesion state. DLS measurements were performed by using an ALV/CGS-3 DLS/SLS Laser Light Scattering Goniometer System (ALV, Langen, Germany). The setup is equipped with a 22 mW polarized HeNe-Laser operating at a wavelength of $\lambda = 632.8$ nm (model 1145P; Uniphase, St. Charles, IL) and an ALV-7004 Multiple Tau Digital Correlator. Data analysis was performed with the ALV-Correlator Software (ALV-7004 for Windows, V.3.0.5.4; ALV, Langen, Germany), as previously described in (20).

### Protein expression and purification

Expression and purification of SNAREs were performed by following the protocol in (3). The SNAREs used in this work, synaptobrevin-2 (residues 1–116 (21) and 49–96 (22)), syntaxin-1A (residues 183–288) (21), and a

cysteine-free variant of SNAP-25A (residues 1–206) (23), were derived from *Rattus norvegicus* and their constructs were cloned into expression vectors. Full-length syb(1–116) C28S was cloned into a pET28a vector containing $His_6$-tags. For the ΔN-complex (containing syb2(49–96), syx1A(183–288) and SN25(1–206)), the SNAREs were coexpressed using the pETDuet-1 vector for syb2(49–96) and syx1A(183–288) and the pET28a vector for SN25(1–206). All SNAREs were expressed in *Escherichia coli* strain BL21(DE3) and purified by $Ni^{2+}$-NTA (nickel-nitrilotiacetic acid) affinity chromatography, followed by ion-exchange chromatography on the Äkta system (GE Healthcare, Little Chalfont, UK). $His_6$-tags were removed by thrombin cleavage.

## Preparation of SNARE-liposomes

The SNARE-liposomes were prepared by following the protocol in (3). Briefly, DOPC:DOPE:DOPS:Chol (molar ratio of 5:2:2:1) liposomes were prepared in a 150 mM KCl, 20 mM HEPES (pH 7.4) buffer by reverse-phase evaporation and subsequently by extrusion through polycarbonate membranes. The lipids were dissolved in chloroform:methanol (2:1) and mixed at the desired molar ratio. Using a rotary evaporator, the solvent was evaporated resulting in a dried lipid film. The lipid film was re-dissolved in 1.5 mL diethyl ether, and 0.5 mL of the buffer was added. The resulting mixture was sonicated using a thin-tip sonicator (Branson Sonifier, 50% duty cycle at low intensity, 3 × 45 s and cooling on ice after each sonification step for 45 s). Diethyl ether was removed from the emulsion by again using the rotary evaporator. Further buffer was added to the resulting liposome suspension to get a final lipid concentration of 8 mM. To get unilamellar liposomes with a mean radius of ∼50 nm, the liposomes were extruded through polycarbonate membranes with a pore size of 0.4 μm and with a pore size of 0.1 μm (each 25 times) in that order.

For SNARE reconstitution, the liposomes were mixed with n-OG (n-octyl-β-D-glucoside) and either with syb or the ΔN-complex purified in 1% n-OG or 3-([3-cholamidopropyl]dimethylammonio)-1-propanesulfonate, respectively. The molar ratios of these mixtures were determined by the *R*-value, which describes the ratio of the concentration of n-OG above its critical micelle concentration to the concentration of the lipids (for details, see (3)), and further by the lipid-to-protein ratio. For reconstitution of the ΔN-complex and of syb, the *R*-values were set to $R = 2$ and to $R = 1.5$, respectively, and the lipid-to-protein ratio was set to 500:1 at a final lipid concentration of 4 mM for both reconstitutions. To remove excess n-OG, two runs of dialysis against liposome buffer using Slide-A-Lyzer cassettes (Thermo Fisher Scientific, Waltham, MA) of a molecular weight cutoff of 2 kDa were performed at room temperature. In a first "overnight" dialysis, 2 g/L of adsorbent beads (SM-2-Bio-Beads; Bio-Rad, Hercules, CA) were included, followed by a second run for ∼4 h.

## SAXS

SAXS experiments were performed at the bending magnet beamline BM29 (BioSAXS) at the European Synchrotron Radiation Facility (ESRF) in Grenoble, France (24). The photon energy was set to $E = 12.5$ keV by a multilayer monochromator with $\Delta E/E \simeq 0.01$. The beam size at the sample plane was (700 × 700) $\mu m^2$. The scattered x rays were recorded using a pixel detector (Pilatus 1M; Dectris, Baden-Dättwil, Switzerland) with 981 × 1043 pixels of size (172 × 172) $\mu m^2$ at a sample-to-detector distance of 2.867 m to cover a *q*-range of ∼0.036–4.95 $nm^{-1}$. By using the sample-changer robot, the samples were automatically loaded into a vacuum-mounted quartz-capillary of 1.8 mm in diameter for exposure. For this purpose, the samples were loaded into PCR tubes (in general 50 μL per sample), and the matched buffers were loaded into microcentrifuge tubes (1–2 mL). For data acquisition, 10 frames of 1 s were recorded for each sample, in which a flow of the sample through the beam was generated to minimize radiation damage. For background subtraction, the matched buffer was measured before and after each sample. Automatic raw data processing, including azimuthal integration to obtain the one-dimensional scattering curve $I(q)$, background subtraction, and curve averaging (with a veto in case of radiation damage), was performed online by a processing pipeline within the *EDNA* framework (25).

## Form and structure factor models

SAXS analysis of lipid vesicles is well-covered in literature. In this work, we largely follow (14,26). However, we briefly repeat the scattering equations for notational clarity and as a basis of the specific choice of model and parameterizations used for the adhesion (docking) state. We use the standard decomposition of the powder-averaged kinematic structure factor $S(q)$ and vesicle (or bilayer) form factor $F(q) = |f(q)|^2$ with the form-factor amplitude $f(q)$ to write the scattering intensity $I(q) \propto \langle F(\vec{q})S(\vec{q})\rangle$, where $\langle\ldots\rangle$ denotes the powder average. $q$ is given by the modulus of the momentum transfer vector $q = |\vec{q}| = (4\pi/\lambda)\sin\theta$, where $\lambda$ is the wavelength of the x rays and $\theta$ the half of the scattering angle relative to the incident beam (cf. Fig. 1). The EDP normal to the bilayer, which enters into the form factor $F(q)$, is parameterized by three Gaussian functions according to

$$\rho(\vec{r}) = \sum_{i=1}^{3} \rho_i \exp\left[-\frac{(z - z_i)^2}{2\sigma_i^2}\right], \tag{1}$$

representing both headgroup regions and the hydrophobic chain region with the amplitude $\rho_i$, the peak position $z_i$, and the width $\sigma_i$ of the respective Gaussian function as sketched in Fig. 1 *b*. This model has the advantage that it provides analytic solutions for $F(q)$.

### The flat bilayer and the spherical vesicle model

For noninteracting vesicles, we assume $S(q) = 1$. We consider two basic models to calculate $F(q)$ on the basis of (14), namely, the flat bilayer model, which assumes that the SAXS signal is dominated by the powder-averaged bilayer structure, and the spherical vesicle model, which takes interference of the bilayer with the overall spherical shape properly into account. Note that the latter has the advantage of providing the mean vesicle radius $R_0$ and polydispersity $\sigma_R$ in addition to the bilayer structure parameters.

With the assumption that interference between different bilayer patches averages out in polydisperse ensembles, the vesicle suspension can be considered as a "perfect powder" of flat lipid bilayer patches with random orientations. The form-factor amplitude is hence given by the one-dimensional Fourier transform of the electron density $\rho(z)$ (Eq. 1),

$$f_{\mathrm{fb}}(q) = \int \rho(z)\exp(\mathrm{i}qz)\mathrm{d}z, \tag{2}$$

followed by powder averaging. The scattering intensity is then simply given by $\langle |f_{\mathrm{fb}}(q)|^2 \rangle$ because interactions between vesicles are neglected (14):

$$I_{\mathrm{fb}}(q) \propto \frac{1}{q^2} \sum_{i=1}^{N}\sum_{j=1}^{N} \rho_i\rho_j\sigma_i\sigma_j \exp\left[-\frac{q^2\left(\sigma_i^2 + \sigma_j^2\right)}{2}\right] \times \cos\left[q\left(z_i - z_j\right)\right], \tag{3}$$

where the factor $q^{-2}$ takes into account the powder average of the one-dimensional Fourier transform in Eq. 2.

Spherical vesicle model: taking the spherical symmetry of the vesicles into account, the form-factor amplitude is given by the radially symmetric Fourier transform of the electron density $\rho(z)$,

$$f_{sv}(q) = \int \rho(r) r^2 \frac{\sin(qr)}{qr} dr. \quad (4)$$

The scattering intensity is then calculated by taking the polydispersity of the vesicle suspension into account using a Gaussian distribution. As shown by (14), it can be written as

$$I_{sv}(q) \propto \frac{1}{q^2} \sum_{i=1}^{N} \sum_{j=1}^{N} \rho_i \rho_j \sigma_i \sigma_j \exp\left[ -\frac{q^2\left(\sigma_i^2 + \sigma_j^2\right)}{2} \right] \times \left[A_{ij}(q) - B_{ij}(q) + C_{ij}(q)\right], \quad (5)$$

where $A_{ij}(q)$, $B_{ij}(q)$, and $C_{ij}(q)$ contain the structural parameters $R_0$ (mean radius) and $\sigma_R$ (standard deviation of the size distribution) as follows:

$$A_{ij}(q) = \left[(R_0 + z_i)(R_0 + z_j) + \sigma_R^2\right] \cos\left[q(z_i - z_j)\right], \quad (6)$$

$$B_{ij}(q) = \exp\left(-2q^2\sigma_R^2\right)\left[(R_0 + z_i)(R_0 + z_j) + \sigma_R^2 - 4q^2\sigma_R^4\right] \cos\left[q(2R_0 + z_i + z_j)\right], \quad (7)$$

and

$$C_{ij}(q) = 2q\sigma_R^2 \exp\left(-2q^2\sigma_R^2\right)(2R_0 + z_i + z_j) \sin\left[q(2R_0 + z_i + z_j)\right]. \quad (8)$$

### The docking model

According to the flat bilayer model, the form-factor amplitude of the electron density of a single bilayer is calculated by the Fourier transform in Eq. 2, yielding (26)

$$f_{fb}(q) = \sqrt{2\pi}\left[ \underbrace{2\sigma_h \rho_h \exp\left(-\frac{\sigma_h^2 q^2}{2}\right)\cos(q z_h)}_{\text{Bilayer headgroups}} + \underbrace{\sigma_c \rho_c \exp\left(-\frac{\sigma_c^2 q^2}{2}\right)}_{\text{Bilayer chain region}} \right]. \quad (9)$$

Here, the left term in the square brackets corresponds to the form factor of the bilayer headgroups and the right term to the form factor of the chain region.

In real space, two bilayers in close apposition can be described by a convolution of the electron density $\rho(z)$, with the sum of two Dirac delta functions with distance $d$ given by

$$s(z) = \delta(z) + \delta(z - d). \quad (10)$$

The Fourier transform of the delta function is simply a shift in Fourier space, thus

$$s(q) = 1 + \exp(-iqd). \quad (11)$$

The modulus square of Eq. 11 gives the structure factor

$$S(q) = 2 + 2\cos(qd). \quad (12)$$

Note that the structure factor in Eq. 12 can also be obtained from a multilamellar vesicle model with $N$ bilayers with periodicity $d$ (26,27), setting $N = 2$. Using Eqs. 9 and 12, the scattering intensity $I(q)$ is given by

$$I_d(q) \propto \frac{1}{q^2}\left[\nu_d \left|f_{fb}(q)\right|^2 S(q) + (1 - \nu_d)\left|f_{fb}(q)\right|^2\right], \quad (13)$$

taking into account the superposition of the scattering contribution of single (undocked) bilayers $(1 - \nu_d)\left|f_{fb}(q)\right|^2$ and of docked bilayers, respectively. Note that even if all vesicles dock, $\nu_d < 1$, corresponding to the fraction of vesicle surface involved in adhesion. Again, the factor $q^{-2}$ takes the powder average into account.

### Form and structure factor simulations

Fig. 2 shows simulated SAXS curves $I(q)$ versus $q$ of the form and structure factor models discussed above to illustrate the characteristic features related to the structural parameters.

In (*a*), we compare the flat bilayer model and the spherical vesicle model. Differences are observed in particular in the low $q$-region, where modulations are evident in the case of the spherical model. Accordingly, this $q$-region is sensitive to the mean radius $R_0$ and to the width of the size distribution $\sigma_R$ of the vesicles. Contrarily, at higher $q$-values, the flat bilayer model represents a good approximation and can be used to obtain structural parameters only of the bilayer in a robust manner. In (*b*), we compare spherical model curves for different radii, whereas the ratio of the radius to the polydispersity is kept constant. As expected, the minima (modulations) are shifted toward lower $q$-values when $R_0/\sigma_R$ increases. Furthermore, we observe an increase of the scattering intensity over the entire $q$-range. In (*c*), we compare scattering curves for different values of $(1 - \nu_d)$. $(1 - \nu_d) = 0$ gives the limiting case for the scattering arising only from adhering bilayers (*blue line*), thus $I_d(q) \propto (1/q^2)F(q)S(q)$. In addition to the form-factor minima of a single bilayer, further modulations are observed because of the structure factor. In the limiting case $(1 - \nu_d) = 1$ (*green line*), the docking model equals the flat bilayer model $I_d(q) \propto (1/q^2)F(q)$. The third example shown is $(1 - \nu_d) = 0.5$ (*orange line*), corresponding to a superposition of the scattering from two bilayers in close apposition and from single uncorrelated bilayers. In this scenario, which corresponds to the experimental observations, the structure-factor modulations can be observed but are less pronounced than the form-factor minima. In (*d*), scattering curves for different water spacings $d_w$ are compared. Although the form-factor minima remain, the intermediate modulations of the structure factor vary in a characteristic manner with $d_w$. As expected, the minima of the structure-factor modulations are shifted toward lower $q$-values when $d_w$ increases.

### Least-squares fitting

To obtain structural parameters from SAXS data, the experimental scattering intensities $I_{exp}(q_i)$ with data points $i = 1, \ldots, N$ recorded at $q_i$ were fitted by the model curve $I_{mod}(q_i)$, accounting for scaling factor and background (additional background contribution after experimental background reduction) as

$$I_{tot}(q) = c_1 \cdot I_{mod}(q) + I_{bg}(q). \quad (14)$$

The quality of the fit was monitored by the reduced $\chi^2$-function

$$\chi^2_{red} = \frac{\sum_{i=1}^{N} \frac{\left[I_{exp}(q_i) - I_{tot}(q_i)\right]^2}{\sigma_i^2}}{N - p - 1}, \quad (15)$$

where $p$ is the number of free model parameters and $\sigma_i^2$ is the variance of the intensity $I_{exp}(q_i)$ for a measured data point $i$. Nonlinear least-squares fitting

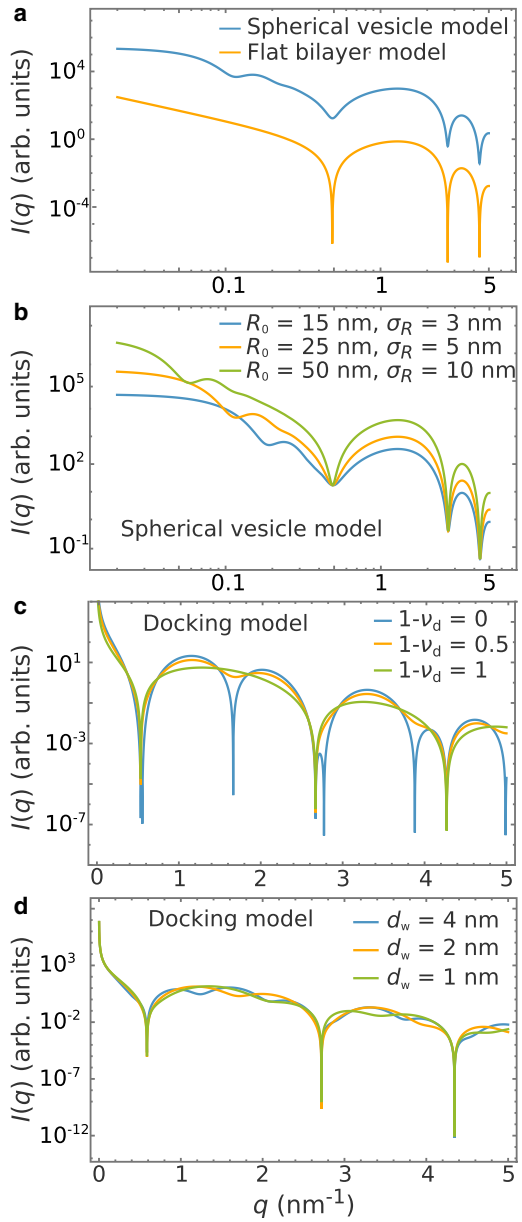


FIGURE 2 Form and structure factor models. (*a*) A comparison of the spherical vesicle model (*blue line*) and the flat bilayer model (*orange line*) is shown. (*b*) The data for the spherical vesicle model for varied radius and polydispersity ($R_0/\sigma_R$ = constant) are shown. (*c*) The data for the docking model for $d_w = 2$ nm and different values of $(1 - \nu_d)$ are shown. (*d*) The data for the docking model for different water spacings $d_w$, 4 nm (*blue line*), 2 nm (*orange line*), and 1 nm (*green line*), for $\nu_d = 0.5$, are shown. The bilayer parameters are $\sigma_h = 0.35$ nm, $\sigma_c = 0.7$ nm, $\rho_h = 1.5$ (arb. units), $\rho_c = -1$ (arb. units), and $d_{hh} = 3.6$ nm for (*a* and *b*) and $\sigma_h = 0.4$ nm, $\sigma_c = 0.7$ nm, $\rho_h = 1.5$ (arb. units), $\rho_c = -1$ (arb. units), and $d_{hh} = 3.66$ nm for (*c* and *d*). To see this figure in color, go online.

was implemented using the MATLAB function *lsqnonlin* of the MATLAB R2016a Optimization Toolbox (MathWorks, Natick, MA).

For the flat bilayer model and the docking model, a constant background $I_{bg}(q) = c_2$ was used to account for possible errors in the instrumental background subtraction. For the spherical vesicle model, both constant and power-law background correction terms $I_{bg}(q) = c_2 q^{-c_3} + c_4$ were used as indicated. For the bilayer structure, a symmetric profile was enforced, reducing the number of free parameters, unless specified otherwise. The Gaussian parameters representing the headgroups are $\sigma_h = \sigma_{h1} = \sigma_{h2}$ and $\rho_h = \rho_{h1} = \rho_{h2}$. Although the width $\sigma_c$ of the Gaussian representing the chain region is a free parameter, the amplitude and the position were fixed to $\rho_c = -1$ (arbitrary (arb.) units) and $z_c = 0$ (nm), respectively. The positions of the two outer Gaussians are denoted as $z_{h1,2} = \pm z_h$. Only for the comparison in Fig. 3, an asymmetric bilayer model was included. Hence, the width and the amplitude of the Gaussians representing the headgroups were free parameters for both sides ($\sigma_{h1} \neq \sigma_{h2}$ and $\rho_{h1} \neq \rho_{h2}$), whereas the positions were fixed analogously to the symmetric profile.

## RESULTS AND DISCUSSION

### SAXS characterization of unilamellar vesicles

First, we have verified that a unilamellar state has been reached by the vesicle preparation for each of the different lipid compositions to have a structural reference for any further docking or fusion reactions. In view of a fusion reaction, we further addressed the question of whether we can control the size distribution of the vesicles. To this end, SAXS measurements were performed after the respective preparation step (subsequent extrusion through membranes of 100, 50, and 30 nm pore size) in ultrapure (Milli-Q) water and are shown as Fig. S2. The SAXS curves indicate that vesicles containing the negatively charged lipid DOPS achieve unilamellarity already after the first preparation step of direct sonication, whereas DOPC:DOPE mixtures (pure DOPC and the molar ratios of 4:1 and 1:1) differ from the characteristic SAXS profile of unilamellar vesicles, in particular between the first two form-factor minima, where remnants of Bragg peaks or at least modulations are observed. For both DOPC and DOPC:DOPE (4:1), unilamellarity is not even achieved after three runs of extrusion (using pore diameters of 100, 50, and 30 nm), whereas DOPC:DOPE (1:1) does become unilamellar after the final extrusion step (30 nm diameter). Hence, if no charged lipid component is used, at least a high molar ratio of DOPE should be used to achieve unilamellar vesicles. A strong decrease in scattering intensity is observed for DOPC and DOPC:DOPE after extrusion, reflecting the significant reduction in lipid concentration after filtering out big aggregates.

Next, we have to select a suitable scattering model for unilamellar vesicles to extract structural parameters of the bilayer EDP. To this end, we compare the models of the flat bilayer dispersion and of perfectly spherical vesicles. We further investigate the effects of constraining the model to asymmetric EDP versus a freely parameterized EDP.

Fig. 3 shows a quantitative analysis of the SAXS data of 30-nm extruded DOPC:DOPE (1:1) vesicles in which different models are compared. In (*a*), the spherical vesicle model and the flat bilayer model fits are shown both for symmetric and asymmetric EDP. For the spherical vesicle model fit, the full $q$-range was fitted, whereas only a restricted $q$-range of ~0.36–4.95 nm$^{-1}$ was fitted to the flat bilayer model, corresponding to the validity of this model

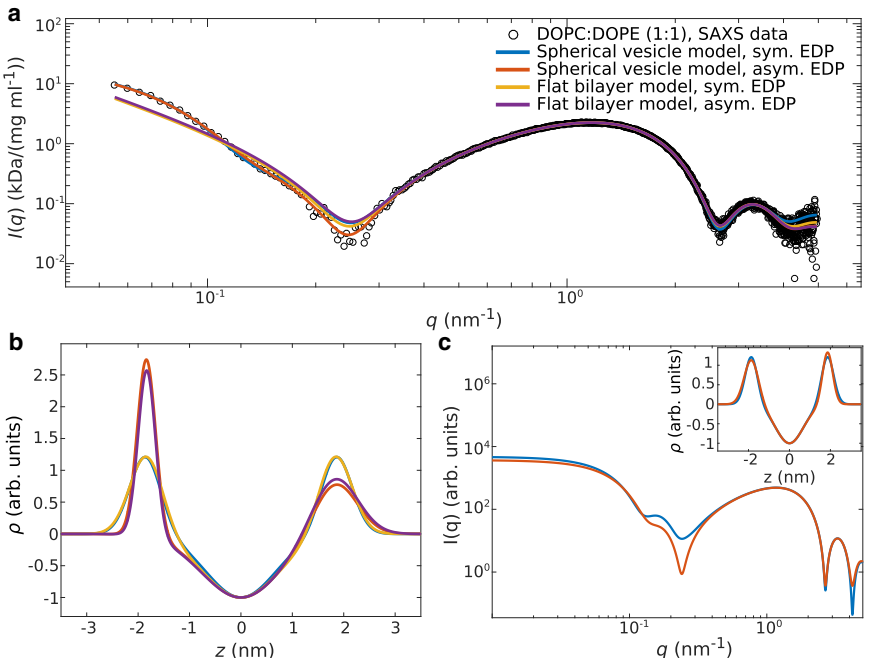


FIGURE 3 (*a*) SAXS data of 30-nm extruded DOPC:DOPE (1:1) vesicles in Milli-Q water (*black circles*), spherical vesicle model fits with either a symmetric or an asymmetric EDP (*blue* and *red lines*, respectively), and flat bilayer model fits with either a symmetric or an asymmetric EDP (*yellow* and *purple lines*, respectively). (*b*) EDPs obtained from the fits in (*a*) with the corresponding colors are shown. (*c*) SAXS simulation results using the spherical vesicle model with either a symmetric or an asymmetric EDP (*blue* and *red*, respectively) are shown. To see this figure in color, go online.

(cf. SAXS simulations, Fig. 2). Note that all fit functions are plotted over the entire $q$-range for a better comparability. Further, an additional power law $c_2 q^{-c_3} + c_4$ modeling the background is included in the spherical vesicle model and a constant background in the flat bilayer model. The dependence of the structural parameters on the choice of the background model is further elucidated in Fig. S3.

The corresponding EDPs are plotted in (*b*). The structural parameters and the related $\chi^2_{red}$ are listed in Table 1. In general, all models match the data quite well, with only minor differences in the medium and high $q$-range. The parameters of the bilayer profile are found to be robust with respect to the two models and background choices. Larger differences between the models are observed in the lower $q$-range. As expected, only the spherical vesicle model can capture the dip corresponding to the vesicle size (radius $R_0$). The values for $R_0$ derived from the fit match the expectation according to the pore size of the extrusion, see Table 1.

Slight improvements of $\chi^2_{red}$ appear for an asymmetric bilayer profile. However, this is hard to justify in view of the unreasonably strong asymmetry (*b*), as well as the high number of free model parameters. In (*c*), SAXS simulations of the spherical vesicle model with either a symmetric or an asymmetric bilayer profile are indicated. The EDP is displayed in the inset. By comparison of the two cases, we observe that already a slightly asymmetric profile yields large deviations in the SAXS profile (*red lines*), in particular for the form-factor minima. This observation indicates that a precise background subtraction is essential when considering an asymmetric bilayer structure, especially because the form-factor minima are sensitive to this. Therefore, we restrict ourselves mainly to the analysis of a symmetric bilayer profile to obtain robust effective EDPs.

Note that the analysis of further curves is presented as Fig. S4, along with tabulated values of structural parameters (Tables S1–S3) obtained from the fits for the respective models.

## Adhesion of lipid vesicles

Next, we have investigated the structural changes induced by the addition of divalent salts. Fig. 4, *a–c* shows a series of SAXS data $I(q)$ versus $q$ of vesicles, either suspended in

**TABLE 1 Structural Parameters Obtained from Spherical Vesicle Model and Flat Bilayer Model Least-Squares Fits to SAXS Data of 30-nm Extruded DOPC:DOPE 1:1 Vesicles Using Either a Symmetric or an Asymmetric Bilayer Profile**

| Model | Bilayer Structure | $\rho_{h1}$, $\rho_{h2}$ (Arb. Units) | $\sigma_{h1}$, $\sigma_{h2}$ (nm) | $\sigma_c$ (nm) | $d_{hh}$ (nm) | $R_0$ (nm) | $\sigma_R$ (nm) | $\chi^2_{red}$ |
|---|---|---|---|---|---|---|---|---|
| Flat bilayer | symmetric | 1.26, 1.26 | 0.32, 0.32 | 0.73 | 3.68 | – | – | 1.15 |
| | asymmetric | 2.63, 0.92 | 0.17, 0.44 | 0.77 | 3.66 | – | – | 1.1 |
| Spherical vesicle | symmetric | 1.23, 1.23 | 0.30, 0.30 | 0.67 | 3.72 | 14.35 | 7.4 | 1.42 |
| | asymmetric | 2.79, 0.82 | 0.18, 0.42 | 0.75 | 3.68 | 15.32 | 8.68 | 1.09 |

The structural bilayer parameters are $\rho_h = \rho_{h1} = \rho_{h2}$ and $\sigma_h = \sigma_{h1} = \sigma_{h2}$ or $\rho_{h1} \neq \rho_{h2}$ and $\sigma_{h1} \neq \sigma_{h2}$ for a symmetric or an asymmetric bilayer profile, respectively. The amplitude of the Gaussian representing the chain region is selected to $\rho_c = -1$ (arb. units) for all fits.

ultrapure water (*a* and *b*) or in a 100 mM glucose solution (*c*), in which structural changes were induced as a function of lipid composition and $CaCl_2$/$MgCl_2$. In the case of pure DOPS (*a*), we observe a phase transition toward a multilamellar phase already at low $CaCl_2$ concentrations, e.g., 0.1 mM, as is evidenced by the emerging Bragg peaks. The latter become more pronounced with an increase of the $CaCl_2$ concentration. From the position of the first Bragg peak, we infer a lamellar periodicity $d = 2\pi/q_0 \approx 4.97$ nm for the 1 mM $CaCl_2$ curve, yielding a water layer thickness $d_w = d - d_{hh} = 1.18$ nm, given the measured headgroup-to-headgroup distance $d_{hh} = 3.79$ nm (Table S1).

Contrary to DOPS, the SAXS profiles of the two-component mixture DOPC:DOPS (1:1) (*b* and *c*) exhibit a different line shape with structure factor modulations instead of Bragg peaks upon addition of $CaCl_2$ or $MgCl_2$ (highlighted by *black arrows*). According to the simulations of the docking model in Fig. 2, we identify these profiles as stable adhesion states of the vesicles. Control experiments indicate that the observed structure factor modulations are characteristic for the divalent cations $Ca^{2+}$ and $Mg^{2+}$. The addition of 4 mM glucose (*b*) or 4 mM KCl (*c*) does not lead to this particular line shape. At the same time, changes in the low *q*-range of the SAXS profile are observed for vesicles suspended in ultrapure water, both for the control experiment as well as upon the addition of $CaCl_2$, indicating structural changes of the vesicle shape, e.g., because of osmotic shrinkage or locally flattened bilayers. Contrarily, no pronounced changes in the low *q*-range are observed for vesicles suspended in a 100 mM glucose solution, indicating that the overall vesicle shape (apart from the contact zone) remains spherical in this case. To shed further light on the overall size of the adhering vesicles, DLS measurements were performed before and after addition of $CaCl_2$. Fig. 4 *d* shows the resulting size distributions for DOPC:DOPS (1:1) vesicles in 100 mM glucose. Upon addition of 4 and 10 mM $CaCl_2$, the size distributions are systematically broadened, particularly toward higher hydrodynamic radii. In this range, the size distributions are still monodisperse, indicating that strong aggregation of many vesicles does not play a role. For 20 mM $CaCl_2$, however, the size distribution becomes bimodal and shifts to significantly higher hydrodynamic radii.

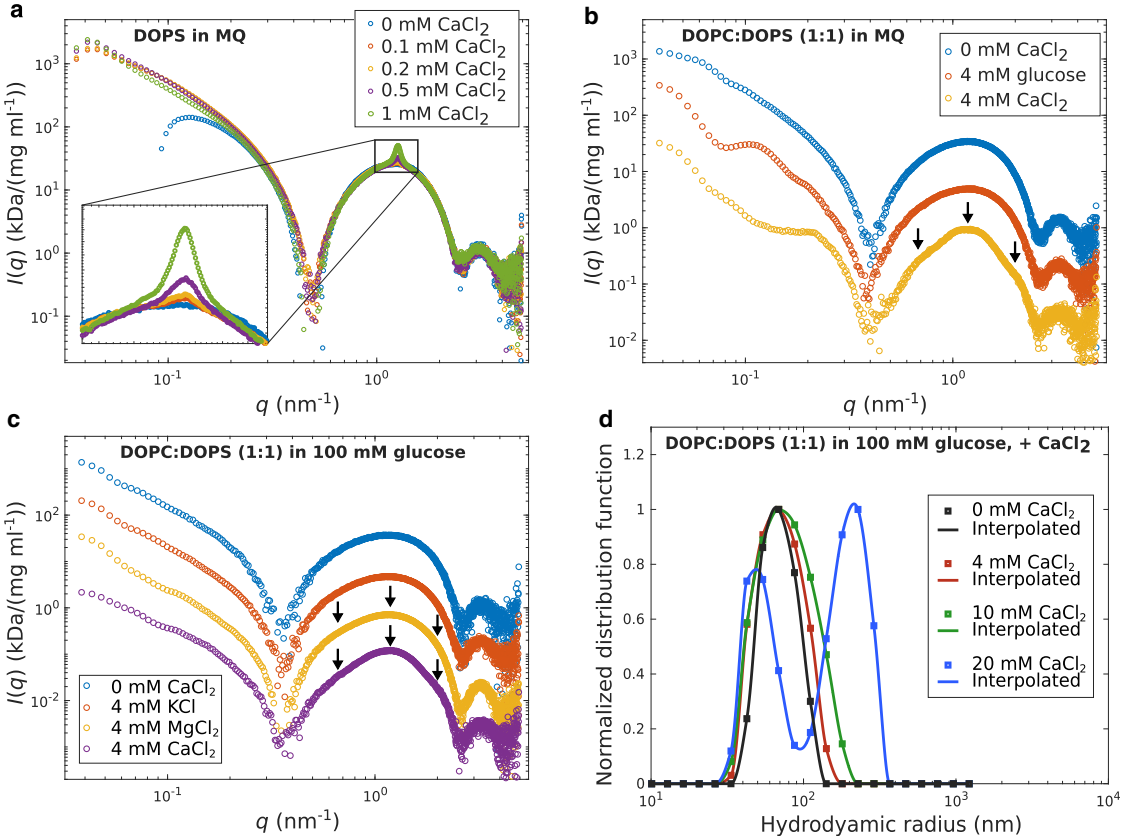


FIGURE 4 (*a*) SAXS data $I(q)$ versus $q$ of DOPS vesicles in ultrapure water, measured after the addition of $CaCl_2$ at different concentrations. (*b*) SAXS data $I(q)$ versus $q$ of DOPC:DOPS (1:1) vesicles in ultrapure water (*blue*), after addition of 4 mM glucose (*red*) and after addition of 4 mM $CaCl_2$ (*yellow*), are shown. The SAXS profiles are shifted for clarity. (*c*) SAXS data $I(q)$ versus $q$ of DOPC:DOPS (1:1) vesicles in a 100 mM glucose solution (*blue*), after addition of 4 mM KCl (*red*), after addition of 4 mM $MgCl_2$ (*yellow*), and after addition of 4 mM $CaCl_2$ (*purple*), are shown. The SAXS profiles are shifted for clarity. (*d*) The size distributions of DOPC:DOPS (1:1) vesicles in 100 mM glucose, measured by DLS after the addition of $CaCl_2$ at different concentrations, are shown. To see this figure in color, go online.

The quantification of structural parameters by least-squares fitting is exemplified in Fig. 5 for $CaCl_2$-induced adhesion of DOPC:DOPS (1:1) vesicles in 100 mM glucose. To this end, the docking model has been applied with a constant background model. As is apparent from (*a*), the docking model is well suited to describe the SAXS data in the fitted $q$-range, here ~0.424–4.95 $nm^{-1}$, in which the scattering is dominated by the bilayer form factor. In (*b*), the corresponding EDP of the two bilayers in close proximity is displayed, with an interbilayer spacing of $d_w = 1.56$ nm. In Table 2, the structural parameters of all fits are listed. Lipid composition, aqueous environment (ultrapure water versus 100 mM glucose solution), and the $CaCl_2$/$MgCl_2$-concentration have been varied. From the results, we draw the following conclusions: 1) the bilayer structure and the interbilayer distance $d_w$ are nearly identical for the glucose solution and ultrapure water; 2) $d_w$ does not change between 4 and 10 mM $CaCl_2$ and $MgCl_2$; 3) $d_w$ for $MgCl_2$ is slightly higher by ~1.5 Å than for $CaCl_2$; 4) in ultrapure water, the vesicles deform more easily than in glucose, favoring a higher fraction of adhered membranes $\nu_d$; and 5) the bilayer thickness increases upon addition of $CaCl_2$ and $MgCl_2$. Note that further EDPs are included as Fig. S5, illustrating the differences between $CaCl_2$- and $MgCl_2$-induced structural changes, as well as the effect of background (monovalent) salt (KCl); see Fig. S6 and Table S4. In this case, higher interbilayer distances (~3–6 nm) are observed.

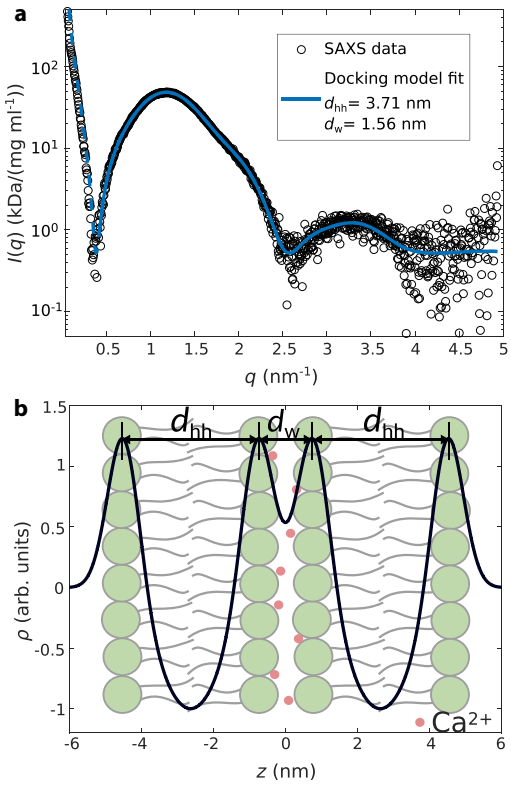


FIGURE 5 (*a*) SAXS data $I(q)$ versus $q$ of DOPC:DOPS (1:1) vesicles suspended in a 100 mM glucose solution upon addition of 4 mM $CaCl_2$ (*black circles*) and least-squares fit using the docking model (*blue line*). (*b*) The reconstructed EDP using the structural parameters obtained from the docking model fit indicated in (*a*) is shown. The structural parameters are summarized in Table 2. To see this figure in color, go online.

## Interaction potentials

Next, we have investigated which additive interaction potentials and parameters could possibly explain the observed values of $d_w \sim 1.6$ nm of the adhesion state. To this end, Fig. 6 shows different approaches for modeling the interaction free energy per unit area corresponding to different experimental scenarios. We start by the "reference state" of uncharged (zwitterionic) phospholipids such as pure DOPC, governed by a repulsive hydration interaction $f_{hyd}$ and an attractive van der Waals term $f_{vdW}$ (28–30). The resulting equilibrium water layer thickness is known from experiments on fully hydrated multilamellar membranes as $d_w \simeq 2.7$ nm (31). Note that the value corresponds to the definition as the distance between the two headgroup maxima. This value is reproduced by modeling the interactions, i.e., by an exponential hydration repulsion term (28)

$$f_{hyd}(d_w) = P_h \lambda_h \exp\left(-\frac{d_w}{\lambda_h}\right), \tag{16}$$

where the prefactor $(P_h \lambda_h)$ is typically on the order of a few $k_B T$ Å$^{-2}$ with the Boltzmann constant $k_B \simeq 1.38065 \times 10^{-23}$ J/K and the temperature $T$, and the decay length $\lambda_h$ is in the range of 1–3 Å. Following (29,32), we write the van der Waals interaction as the sum of the static and the dispersive part $f_{vdW}(d_w) = f_{stat}(d_w) + f_{disp}(d_w)$ with

$$\begin{aligned} f_{vdW}(d_w) = &-\frac{H_{stat} k_B T}{12\pi (d + d_h/2)^2} \\ &-\frac{H_{disp} k_B T}{16\pi (d + d_h)^2}\left[1 - \frac{2}{(1 + d_a/(d + d_h))^2}\right. \\ &\left. + \frac{1}{(1 + 2d_a/(d + d_h/2))^2}\right], \end{aligned} \tag{17}$$

where $d_h$ and $d_a$ denote the hydrophilic and hydrophobic slab thickness, i.e., the headgroup and hydrocarbon chains, respectively. The Hamaker constants $H_{stat}$ and $H_{disp}$ are of order one. The resulting potential is plotted in Fig. 6 *a* for the exact parameter values given in the caption. When anionic lipids such as DOPS are present as in the experimental two-component lipid mixture, the corresponding average surface charge density $\sigma$ results in an unbinding of charged membranes, i.e., the van der Waals attraction cannot compensate for the repulsion in the Poisson-

**TABLE 2 Structural Parameters as Obtained from the Flat Bilayer and Docking Model Analyses of the SAXS Data of DOPC:DOPS 1:1 Vesicles in MQ and in 100 mM Glucose with Respect to the Added $CaCl_2$ and $MgCl_2$ Concentration**

| Sample | Fit Model | [$CaCl_2$] (mM) | [$MgCl_2$] (mM) | $\rho_h$ (Arb. Units) | $\sigma_h$, $\sigma_c$ (nm) | $d_{hh}$ (nm) | $d_w$ (nm) | $(1-\nu_d)$ | $\chi^2_{red}$ |
|---|---|---|---|---|---|---|---|---|---|
| DOPC:DOPS (1:1) in MQ | flat bilayer | – | – | 1.35 | 0.42, 0.89 | 3.64 | – | – | 1.19 |
| | docking | 4 | – | 1.42 | 0.44, 0.95 | 3.72 | 1.54 | 0.85 | 1.37 |
| DOPC:DOPS (1:1) in 100 mM glucose | flat bilayer | – | – | 1.27 | 0.42, 0.90 | 3.63 | – | – | 1.03 |
| | docking | 4 | – | 1.39 | 0.44, 0.95 | 3.71 | 1.56 | 0.89 | 1.14 |
| | docking | 10 | – | 1.26 | 0.51, 0.98 | 3.70 | 1.60 | 0.82 | 0.95 |
| | docking | – | 4 | 1.34 | 0.39, 0.84 | 3.72 | 1.72 | 0.98 | 0.89 |
| | docking | – | 10 | 1.32 | 0.46, 0.98 | 3.69 | 1.74 | 0.86 | 1.11 |

The model fits are based on a symmetric EDP; thus, the amplitude and width of the inner and outer leaflet are $\rho_h = \rho_{h1} = \rho_{h2}$ and $\sigma_h = \sigma_{h1} = \sigma_{h2}$. The amplitude of the Gaussian representing the chain region is selected to $\rho_c = -1$ (arb. units) for all fits.

Boltzmann regime (33). How does this change if salt is added and electrostatic repulsion is screened?

For monovalent ions and concentrations in the experimentally relevant mM range, the repulsion is in the Gouy-Chapman regime. This follows from evaluation of the three characteristic length scales, the Debye screening length $\lambda_D = \left((\varepsilon_0\varepsilon_r k_B T)\left(\sum_i n_{0,i} e^2 q_i^2\right)^{-1}\right)^{1/2}$, the Bjerrum length $l_B = e^2(4\pi\varepsilon\varepsilon_0 k_B T)^{-1}$, and the Gouy-Chapman length $l_{GC} = (2\pi q l_B \sigma)^{-1}$ according to (12,34), for the parameters given in the caption. Here, $e$ is the elementary charge, $q$ is the valency of the ions, $n_0$ is the number density of the ions, $\varepsilon_0 = 8.85 \times 10^{-12}$ F/m is the vacuum permittivity, $\varepsilon_r \simeq 80$ is the dielectric constant for water, and $\sigma$ is the surface charge density in the units of $e/m^3$. In this regime, the free energy per unit area is given by (12,34)

$$f_{GC}(d_w) = \frac{\pi k_B T}{2 l_B d_w}, \tag{18}$$

which is plotted in Fig. 6 *b*, including an additional van der Waals term (*orange line*). Again, no minimum and thus no adhesion state is formed. Only if we introduce an additional osmotic pressure (*red line*) can a minimum again form (*blue line*), albeit at much larger distances for the relevant osmotic pressure corresponding to an excess concentration of ions in the mM range. Such an osmotic pressure or depletion force could arise if ions are expelled from the intermembrane space, similar to the phenomenon reported in (35). Accordingly, we would have an additional attractive interaction

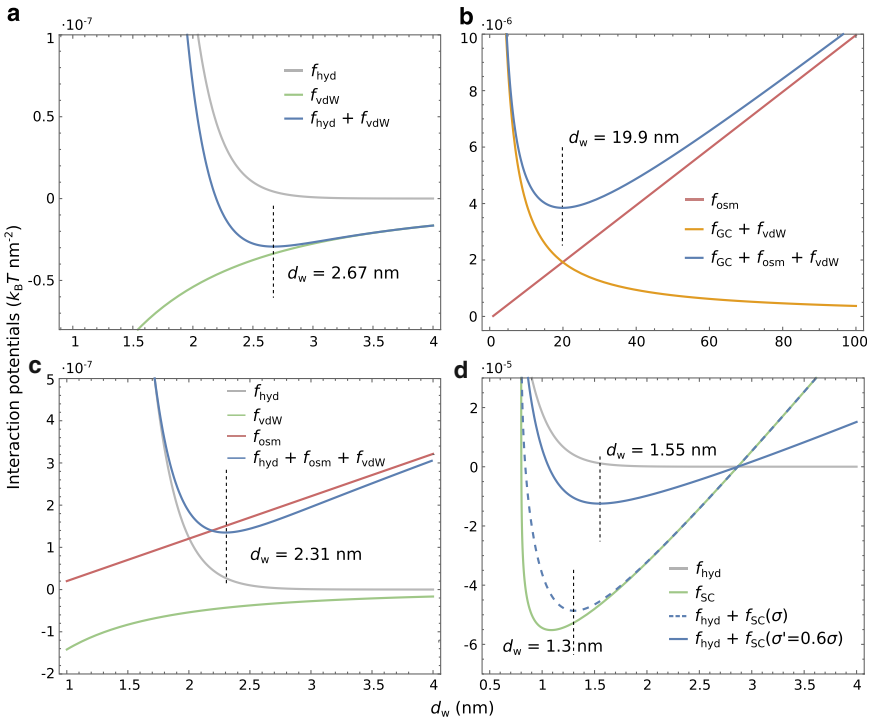


FIGURE 6 Calculated interaction potentials per unit area as a function of the interbilayer distance, modeled to discern possible scenarios to reproduce the experimental equilibrium water layer $d_w \simeq 1.6$ nm in the adhesion state. (*a*) The total interaction potential for uncharged membranes exhibits a local minimum at $d_w \approx 2.7$ nm for the experimental parameters given below. (*b*) The adhesion vanishes if Poisson-Boltzmann repulsion in the Gouy-Chapman regime is taken into account and can be rescued only by an additional (attractive) osmotic pressure, plotted here for an assumed maximum of 10 mM expelled ions causing the attractive osmotic pressure (or depletion force). (*c*) The same depletion force acting on the neutral membrane would only slightly change the adhesion state to $d_w \approx 2.3$ nm. (*d*) The strong coupling potential (*green line*) yields an attractive interaction of like-charge membranes at small separations. By adding the hydration repulsion, an equilibrium water spacing of $d_w \approx 1.3$ nm is found, already close to the experimental finding. The latter is well-reproduced for $\sigma' = 0.6\sigma$ (*solid blue line*). The following simulation parameters have been used: $\sigma = 0.5/64 \times 10^{20}\ e/m^2$ assuming an area per lipid headgroup of 64 Å$^2$, $\lambda_D \simeq 2.36 \times 10^{-9}$ m, $l_B \simeq 7.11 \times 10^{-10}$ m, $l_{GC} \simeq 2.87 \times 10^{-10}$ m in (*b*), $l_{GC} \simeq 1.43 \times 10^{-10}$ m in (*d*), $d_a = 20 \times 10^{-10}$ m, $d_h = 16 \times 10^{-10}$ m, $H_{stat} = 0.7$, $H_{disp} = 0.7$, $\lambda_h = 2 \times 10^{-10}$ m, $P_h = 3.3 \times 10^9$ Jm$^{-3}$, and $T = 294$ K. To see this figure in color, go online.

$$f_{\mathrm{osm}}(d_{\mathrm{w}}) = cRTd_{\mathrm{w}}, \tag{19}$$

where $c$ is the excess concentration of the expelled ions or molecules in the units of mol $m^{-3}$ and $R \approx 8.314$ kg $m^2$ $s^{-2}$ $mol^{-1}$ $K^{-1}$ is the gas constant. Here, we can assume a maximal value of 10 mM for the expelled ions. Such an osmotic pressure would hence result in a rather large $d_{\mathrm{w}}$ in the range of several nm, rescuing a weak adhesion state in charged membranes. Contrarily, it would have only a minor effect on $d_{\mathrm{w}}$ in the uncharged reference system (pure DOPC), as visualized in Fig. 6 *c*, in comparison to (*a*). Accordingly, neither osmotic effects nor mean-field electrostatics (12,34), which neglects ion-ion correlation effects and is also denoted as the weak coupling regime, can explain the experimental results. Contrarily, the so-called strong coupling theory (13,36–38), which is characterized by ion bridging and/or ion correlation effects, is well-known to result in attractive interaction of like-charge membranes. The two regimes are delineated by the unitless coupling parameter $\Xi = \tilde{l}_{\mathrm{B}}/l_{\mathrm{GC}}$, where $\tilde{l}_{\mathrm{B}} = q^2 l_{\mathrm{B}}$. The Poisson-Boltzmann approximation is valid for $\Xi \ll 1$, whereas $\Xi \gg 1$ is denoted as the strong coupling regime. For the present experimental parameters, we indeed find $\Xi \simeq 19.8$. Correspondingly, we must turn to the strong coupling regime, for which an analytical expression was derived in (13,38) in terms of the interaction pressure

$$P_{\mathrm{SC}}(d_{\mathrm{w}}) = 2\pi l_{\mathrm{B}}\sigma^2 k_{\mathrm{B}}T\left(-1 + \frac{2l_{\mathrm{GC}}}{d_w}\right). \tag{20}$$

By integration, we find the potential plotted in (*d*) (*green line*) for the given experimental parameters. The addition of the hydration repulsion to the strong coupling potential (*dashed blue line*) predicts an adhesion state with $d_{\mathrm{w}} \simeq 1.3$ nm, which is already quite close to the experimental finding. Further, a reduction of the charge density to $\sigma' = 0.6\sigma$ (*solid blue line*), or equivalently an increase of the decay length $\lambda_{\mathrm{h}}$ of the hydration repulsion from 0.2 to 0.25 nm (data not shown), would result in perfect agreement. We find that the van der Waals force can be safely neglected here because the attractive force is in this case largely dominated by like-charge attraction, as given by the expression above.

We conclude that the observed adhesion state with $d_{\mathrm{w}} \simeq 1.6$ nm is well explained by a superposition of hydration repulsion and electrostatics in the strong coupling regime predicted by the theory of Netz, Moreira, and coworkers.

### Outlook: SNARE-liposomes

After probing the adhesion state in pure lipid vesicles, the next challenge is to perform similar experiments using proteoliposomes, in which complex formation of SNAREs and $Ca^{2+}$ condensation both control adhesion and subsequently fusion. Although we could not yet reach this goal in this work, we pave the way by a careful structural characterization of the preparation pathway of SNARE-liposomes as displayed in Fig. 7 *a* and *b* to get a better understanding of the structure of SNARE-liposomes. (*a*) shows SAXS data of DOPC:DOPE:DOPS:Chol (5:2:2:1) liposomes in a 150 mM KCl, 20 mM HEPES (pH 7.4) buffer (*blue circles*) and of DOPC:DOPE:DOPS:Chol (5:2:2:1) liposomes after an overnight dialysis, in which the liposomes were mixed with n-OG (*red circles*). For the latter case, the $R$-value was set to $R = 2$ (analogous to the preparation of $\Delta$N-liposomes). The least-squares analysis is based on the spherical vesicle model with an additional power-law background model. Structural parameters of the fits are listed in Table 3. The obtained EDPs are indicated in the inset. We address the question whether an overnight dialysis involving n-OG affects the bilayer structure. In fact, the analysis of both scattering curves reveals significant changes in the bilayer structure as the headgroup-to-headgroup distance $d_{\mathrm{hh}}$ decreases by $\sim$4 Å after the dialysis step. Moreover, the mean radius of the liposome suspension is decreased after dialysis. Fig. 7 *b* shows SAXS data from $\Delta$N- (*red circles*) and SybWT-liposomes (*blue circles*). Compared to the SAXS curves of pure lipid vesicles, the curves differ, particularly in the lower $q$-range. The first minima are less pronounced for SNARE-liposomes, in particular for $\Delta$N-liposomes, most likely due to the interference between the SNAREs and the lipid bilayer as well as the form factor of the SNAREs themselves. Least-squares analysis is carried out based on the flat bilayer model with an additional constant background assuming a symmetric bilayer structure. The corresponding EDPs are shown in the inset, and the structural parameters are listed in Table 3. By comparison of the structural parameters, we observe only slight differences between Syb- and $\Delta$N-liposomes, and between the SNARE-liposomes and the control liposomes (after dialysis). This indicates that the SNAREs have only a minor effect on the mean lipid bilayer structure. For example, for all SNARE-liposomes, a slight increase of $d_{\mathrm{hh}}$ up to $\sim$1 Å was obtained. Hence, rather than a result of SNARE reconstitution, the thinning must be attributed to the preparation protocol. It could be explained either by a loss of Chol (39) washed out by n-OG or by a remaining fraction of n-OG even after dialysis. Note that n-OG is known to form bilayers together with phospholipids (40). Further evidence for the second explanation is found in (11).

## CONCLUSIONS

First, we have screened the preparation pathway and parameters as well as different fitting models in view of structural docking and fusion assays. Suitable suspensions of small unilamellar vesicles were obtained for all but pure DOPC vesicles, which showed interbilayer interactions even after

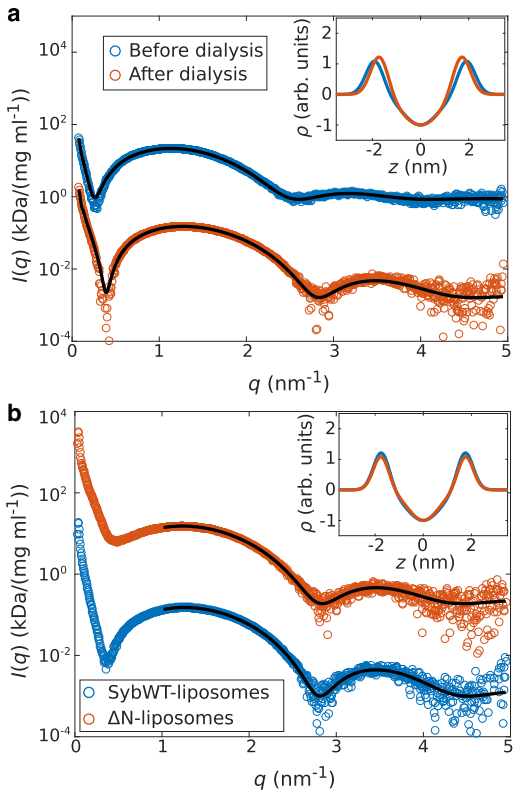


FIGURE 7 Structural characterization of SNARE-liposomes. (*a*) SAXS data of DOPC:DOPE:DOPS:Chol (5:2:2:1) liposomes (shifted for clarity) directly after extrusion (*blue circles*) and after an overnight dialysis, mixed with n-OG ($R = 2$, *red circles*), are shown. Least-squares fits (*black lines*) are based on the spherical vesicle model, and the resulting EDPs are indicated in the inset (colors correspond to the SAXS data). (*b*) SAXS data of SNARE-liposomes, SybWT-liposomes (*blue circles*), and ΔN-complex liposomes (*red circles*), shifted for clarity, are shown. Least-squares fits (*black lines*) are based on the flat bilayer model, and the resulting EDPs are indicated in the inset (colors correspond to the SAXS data). To see this figure in color, go online.

several extrusion steps. In all cases, it was challenging to achieve vesicle preparations with sufficiently small polydispersity $\sigma_R$ to clearly observe $R_0$ and $\sigma_R$. From the spherical vesicle model fits, we have obtained plausible values, for example $R_0 \simeq 14$ nm and $\sigma_R = 7.4$ nm for 30-nm extruded DOPC:DOPE (1:1) vesicles, but it must be realized that a high polydispersity in combination with an insufficient fusion efficiency probably does not allow us to clearly observe the increase in $R_0$ following vesicle fusion. The spherical vesicle model is found to be too restrictive because it does not account for any deviations from the perfect sphere, for example, by thermal fluctuations. Contrarily, the quasi-planar bilayer model was used in a very robust and convincing manner if the low $q$-range is excluded. However, access to $R_0$ is of course lost in this case. In future, there are several possible remedies: 1) the vesicle population could be purified, or the scattering volume could be reduced, e.g., by using microfluidics in combination with focused undulator radiation; 2) the spherical model can be generalized to account for deviations from the perfect spherical shape with appropriate parameters for shape and size polydispersity; and 3) the absolute scattering intensity in combination with calibrated vesicle concentration can be exploited to obtain constraints on $R_0$. Further, MD simulation studies could be used to obtain constraints in the analysis of the SAXS data. It would, for example, be an interesting task to include asymmetric bilayer profiles resulting from curvature (41,42).

As the main result of this work, we found very clear evidence for a calcium-induced adhesion state in lipid vesicles initially suspended in ultrapure water or in a 100 mM glucose solution and could quantify the corresponding density profiles of the contact zone. The control experiments in glucose solution prove that the double bilayer contact detected by the SAXS pattern does not arise from deflated vesicles, but indeed from the adhesion between two different vesicles. Further, the characteristic water layer thickness in this strong adhesion regime was nearly identical for ultrapure water $d_w \approx 1.5 - 1.7$ nm and for the glucose solution and also was nearly identical at 4 and 10 mM concentration of bulk $CaCl_2$. This suggests a recruitment of $Ca^{2+}$ to the contact zone in a quantity required to compensate the charge density of anionic membranes. The monovalent counterions must hence be expelled from the contact zone. The resulting osmotic pressure is not the cause of the adhesion but rather its outcome, and yet may further act to stabilize the adhesion. Given the fact that $d_w$ is defined here as the distance between density maxima of the headgroups, and the headgroup width is $d_h \simeq 0.8$ nm, an ion bridging phenomenon is structurally plausible, eventually accompanied by a local bilayer corrugation. The observed interbilayer distance can also be compared to the critical distance where the stalk phase appears ($0.9 \pm 0.05$ nm), an intermediate before fusion (8).

Using realistic parameters, simple mean field models of electrostatics do not result in interbilayer potentials that yield the observed interbilayer distances. Only when we evaluate the interaction forces of the so-called strong coupling theory according to Netz, Moreira, and coworkers can we reproduce the experimental result for realistic parameters. Accordingly, ion condensation on the bilayer surface and ion correlations are responsible for the observed adhesion. This phenomenon, which is interesting in itself from a soft matter and electrostatics point of view, certainly deserves further attention and should be complemented by investigations of solid-supported lipid bilayers in solution in the presence of $CaCl_2$ (e.g., (43–45)), as well as by MD simulations in the future. Here, we observed nearly the same effect for $Mg^{2+}$ as for $Ca^{2+}$, with a small but systematic shift of $\Delta d_w \simeq 0.15$ nm. This would be in line with recent reports that $Ca^{2+}$ and $Mg^{2+}$ dehydrate and partially neutralize the bilayer surface, with a stronger effect for $Ca^{2+}$ due to a higher binding affinity (19), which could possibly

**TABLE 3 Structural Parameters of Syb- and ⊿N-Liposomes and of Protein-free Liposomes with the Same Lipid Composition DOPC:DOPE:DOPS:Chol 5:2:2:1 with Respect to the Fit Model**

| | Fit Model | $\rho_h$ | $\sigma_h$, $\sigma_c$ | $d_{hh}$ (nm) | $R$ (nm) | $\sigma_R$ (nm) | $\chi^2_{red}$ |
|---|---|---|---|---|---|---|---|
| DOPC:DOPE:DOPS:Chol (5:2:2:1) in buffer | spherical vesicle | 1.12 | 0.36, 0.72 | 3.81 | 47.8 | 17 | 1.39 |
| | flat bilayer | 1.11 | 0.36, 0.70 | 3.83 | – | – | 0.82 |
| DOPC:DOPE:DOPS:Chol (5:2:2:1) in buffer (after dialysis) | spherical vesicle | 1.36 | 0.32, 0.72 | 3.45 | 34.7 | 18.1 | 1.20 |
| | flat bilayer | 1.35 | 0.34, 0.78 | 3.41 | – | – | 0.67 |
| SybWT-liposomes in buffer | flat bilayer | 1.26 | 0.33, 0.71 | 3.47 | – | – | 0.68 |
| SybΔ84-liposomes in buffer | flat bilayer | 1.24 | 0.34, 0.71 | 3.51 | – | – | 0.68 |
| ⊿N-liposomes in buffer | flat bilayer | 1.10 | 0.32, 0.64 | 3.51 | – | – | 0.72 |
| DOPC:DOPE:DOPS:Chol (5:2:2:1) in ultrapure water | spherical vesicle | 1.09 | 0.46, 0.84 | 3.55 | 29.4 | 13.7 | 2.47 |

For all fits, a symmetric bilayer profile was applied so that $\rho_h = \rho_{h1} = \rho_{h2}$ and $\sigma_h = \sigma_{h1} = \sigma_{h2}$. The amplitude of the Gaussian representing the chain region is $\rho_c = -1$ (arb. units) for all fits.

also play a role in the physiological scenario of calcium-dependent membrane fusion. Finally, we observed a stable $CaCl_2$-induced adhesion state at a reduced concentration of monovalent salt, but in a soft regime characterized by much higher interbilayer distances not compatible with ion bridging. Depending on lipid composition and ion concentrations, this equilibrium distance could be varied over a wide range (~3–6 nm), see (Fig. S6; Table S4).

In the future, protein-induced docking should become tractable by the scattering model put forward here once a higher efficiency and purity of the SNARE-induced adhesion state can be reached. As a first step toward this goal, we have structurally characterized vesicles with reconstituted SNAREs in this work. Specifically, our future aim will be to identify and to characterize a SNARE-induced docking state, based on a suitable mutant (Syb⊿84), which prevents full fusion but promotes docking. However, we did not find clear evidence for this state yet, possibly because of limited efficiency and loss of the signal by averaging over different populations (see Fig. S7). Nevertheless, even without docking and fusion, the structural characterization of vesicles with reconstituted SNAREs was successful and is an important first step. Generally, the SAXS data of the SNARE-liposomes showed more features in the scattering curves $I(q)$ versus $q$ (hence, also potentially more information) than we could analyze in this work with limited models. With appropriate extensions of the form-factor models, it should become possible to obtain information on the SNAREs in the lipid bilayers. Given a lipid-to-protein ratio of 500:1, we estimate a copy number of ~70 SNAREs per vesicle with a radius of 30 nm. With a "full $q$-range" model, including a coarse-grained description of the SNAREs, the distribution of SNAREs and possible clustering could be addressed along with the mean radius and the polydispersity of the SNARE-liposomes. Such a model could then be useful to study the structure before and after fusion as well as the arrested docking intermediate. Toward this goal, a first point of reference is the work of Castorph et al. (46), in which anisotropic form factor models were derived for the analysis of SAXS data of synaptic vesicles, including the structure of both the lipid bilayer and the protein layers inside and outside of the vesicles.

## SUPPORTING MATERIAL

Supporting Materials and Methods, seven figures, and four tables are available at http://www.biophysj.org/biophysj/supplemental/S0006-3495(18)30341-2.

## AUTHOR CONTRIBUTIONS

K.K., R.J., and T.S. designed research. K.K., A.S., and H.Y. prepared samples. K.K., A.S., Y.X., and T.S. carried out synchrotron experiments with support and advice from M.B. K.K. analyzed data with support from A.S. and Y.X. and advice from T.S. K.K. and T.S. wrote the manuscript, with comments and critical reading from all authors.

## ACKNOWLEDGMENTS

The SAXS experiments were performed on beamline BM29 at the ESRF, Grenoble, France. We acknowledge Dr. Diego Pontoni, Dr. Yuri Gerelli, and Pierre Lloria for sharing their resources and expertise at ESRF and at the Partnership for Soft Condensed Matter facilities during our beamtimes. We also thank Susanne Hengst for her support in sample preparation and Dr. Sebastian Aeffner and Kilian Frank for fruitful discussions.

This work was supported financially by Sonderforschungsbereich 803, "Functionality Controlled by Organization in and between Membranes," and by Sonderforschungsbereich 937, "Collective behavior of soft and biological matter," funded by Deutsche Forschungsgemeinschaft.

## REFERENCES

1. Takamori, S., M. Holt, …, R. Jahn. 2006. Molecular anatomy of a trafficking organelle. *Cell.* 127:831–846.
2. Jahn, R., and R. H. Scheller. 2006. SNAREs–engines for membrane fusion. *Nat. Rev. Mol. Cell Biol.* 7:631–643.
3. Hernandez, J. M., A. Stein, …, R. Jahn. 2012. Membrane fusion intermediates via directional and full assembly of the SNARE complex. *Science.* 336:1581–1584.
4. Diao, J., P. Grob, …, A. T. Brunger. 2012. Synaptic proteins promote calcium-triggered fast transition from point contact to full fusion. *eLife.* 1:e00109.

5. Grafmüller, A., J. Shillcock, and R. Lipowsky. 2009. The fusion of membranes and vesicles: pathway and energy barriers from dissipative particle dynamics. *Biophys. J.* 96:2658–2675.
6. Risselada, H. J., and H. Grubmüller. 2012. How SNARE molecules mediate membrane fusion: recent insights from molecular simulations. *Curr. Opin. Struct. Biol.* 22:187–196.
7. Yang, L., and H. W. Huang. 2002. Observation of a membrane fusion intermediate structure. *Science.* 297:1877–1879.
8. Aeffner, S., T. Reusch, …, T. Salditt. 2012. Energetics of stalk intermediates in membrane fusion are controlled by lipid composition. *Proc. Natl. Acad. Sci. USA.* 109:E1609–E1618.
9. Khattari, Z., S. Köhler, …, T. Salditt. 2015. Stalk formation as a function of lipid composition studied by X-ray reflectivity. *Biochim. Biophys. Acta.* 1848:41–50.
10. Weinhausen, B., S. Aeffner, …, T. Salditt. 2012. Acyl-chain correlation in membrane fusion intermediates: x-ray diffraction from the rhombohedral lipid phase. *Biophys. J.* 102:2121–2129.
11. Xu, Y., J. Kuhlmann, …, T. Salditt. 2018. Reconstitution of SNARE proteins into solid-supported lipid bilayer stacks and x-ray structure analysis. *Biochim. Biophys. Acta.* 1860:566–578.
12. Andelman, D. 1995. Electrostatic properties of membranes: the Poisson-Boltzmann theory. *In* Handbook of Biological Physics, vol. 1. Structure and Dynamics of Membranes, From Cells to Vesicles. R. Lipowsky and E. Sackman, eds. Elsevier, pp. 603–642.
13. Netz, R. R. 2001. Electrostatistics of counter-ions at and between planar charged walls: from Poisson-Boltzmann to the strong-coupling theory. *Eur. Phys. J. E.* 5:557–574.
14. Brzustowicz, M. R., and A. T. Brunger. 2005. X-ray scattering from unilamellar lipid vesicles. *J. Appl. Cryst.* 38:126–131.
15. Székely, P., A. Ginsburg, …, U. Raviv. 2010. Solution X-ray scattering form factors of supramolecular self-assembled structures. *Langmuir.* 26:13110–13129.
16. Heberle, F. A., J. Pan, …, J. Katsaras. 2012. Model-based approaches for the determination of lipid bilayer structure from small-angle neutron and X-ray scattering data. *Eur. Biophys. J.* 41:875–890.
17. Pannuzzo, M., D. H. De Jong, …, S. J. Marrink. 2014. Simulation of polyethylene glycol and calcium-mediated membrane fusion. *J. Chem. Phys.* 140:124905.
18. Issa, Z. K., C. W. Manke, …, J. J. Potoff. 2010. Ca(2+) bridging of apposed phospholipid bilayers. *J. Phys. Chem. B.* 114:13249–13254.
19. Tsai, H. H., W. X. Lai, …, W. H. Tseng. 2012. Molecular dynamics simulation of cation-phospholipid clustering in phospholipid bilayers: possible role in stalk formation during membrane fusion. *Bochim. Biophys. Acta.* 1818:2742–2755.
20. Castorph, S., S. Schwarz Henriques, …, T. Salditt. 2011. Synaptic vesicles studied by dynamic light scattering. *Eur. Phys. J. E Soft Matter.* 34:63.
21. Schuette, C. G., K. Hatsuzawa, …, R. Jahn. 2004. Determinants of liposome fusion mediated by synaptic SNARE proteins. *Proc. Natl. Acad. Sci. USA.* 101:2858–2863.
22. Pobbati, A. V., A. Stein, and D. Fasshauer. 2006. N- to C-terminal SNARE complex assembly promotes rapid membrane fusion. *Science.* 313:673–676.
23. Fasshauer, D., W. Antonin, …, R. Jahn. 1999. Mixed and non-cognate SNARE complexes. Characterization of assembly and biophysical properties. *J. Biol. Chem.* 274:15440–15446.
24. Pernot, P., A. Round, …, S. McSweeney. 2013. Upgraded ESRF BM29 beamline for SAXS on macromolecules in solution. *J. Synchrotron Radiat.* 20:660–664.
25. Brennich, M. E., J. Kieffer, …, A. Round. 2016. Online data analysis at the ESRF bioSAXS beamline, BM29. *J. Appl. Cryst.* 49:203–212.
26. Pabst, G., M. Rappolt, …, P. Laggner. 2000. Structural information from multilamellar liposomes at full hydration: full q-range fitting with high quality x-ray data. *Phys. Rev. E Stat. Phys. Plasmas Fluids Relat. Interdiscip. Topics.* 62:4000–4009.
27. Heftberger, P., B. Kollmitzer, …, G. Pabst. 2013. Global small-angle X-ray scattering data analysis for multilamellar vesicles: the evolution of the scattering density profile model. *J. Appl. Cryst.* 47:173–180.
28. Israelachvili, J. N., and H. Wennerstroem. 1992. Entropic forces between amphiphilic surfaces in liquids. *J. Phys. Chem.* 96:520–531.
29. Mennicke, U., D. Constantin, and T. Salditt. 2006. Structure and interaction potentials in solid-supported lipid membranes studied by X-ray reflectivity at varied osmotic pressure. *Eur. Phys. J. E Soft Matter.* 20:221–230.
30. Petrache, H. I., N. Gouliaev, …, J. F. Nagle. 1998. Interbilayer interactions from high-resolution x-ray scattering. *Phys. Rev. E.* 57:7014–7024.
31. Tristram-Nagle, S., H. I. Petrache, and J. F. Nagle. 1998. Structure and interactions of fully hydrated dioleoylphosphatidylcholine bilayers. *Biophys. J.* 75:917–925.
32. Fenzl, W. 1995. Van der Waals interaction of membranes. *Z. Phys. B. Con. Mat.* 97:333–336.
33. Demé, B., M. Dubois, …, T. Zemb. 2002. Giant collective fluctuations of charged membranes at the lamellar-to-vesicle unbinding transition. 1. Characterization of a new lipid morphology by SANS, SAXS, and electron microscopy. *Langmuir.* 18:997–1004.
34. Markovich, T., D. Andelman, and R. Podgornik. 2016. Charged membranes: Poisson-Boltzmann theory, DLVO paradigm and beyond. *arXiv*, arXiv:1603.09451v2.
35. Hishida, M., Y. Nomura, …, K. Saito. 2017. Electrostatic double-layer interaction between stacked charged bilayers. *Phys. Rev. E.* 96:040601.
36. Moreira, A. G., and R. R. Netz. 2001. Binding of similarly charged plates with counterions only. *Phys. Rev. Lett.* 87:078301.
37. Moreira, A. G., and R. R. Netz. 2002. Simulations of counterions at charged plates. *Eur. Phys. J. E. Soft Matter.* 8:33–58.
38. Naji, A., S. Jungblut, …, R. R. Netz. 2005. Electrostatic interactions in strongly coupled soft matter. *Physica A.* 352:131–170.
39. Kucerka, N., J. Pencer, …, J. Katsaras. 2007. Influence of cholesterol on the bilayer properties of monounsaturated phosphatidylcholine unilamellar vesicles. *Eur. Phys. J. E Soft Matter.* 23:247–254.
40. Angelov, B., M. Ollivon, and A. Angelova. 1999. X-ray diffraction study of the effect of the detergent octyl glucoside on the structure of lamellar and nonlamellar lipid/water phases of use for membrane protein reconstitution. *Langmuir.* 15:8225–8234.
41. Kucerka, N., J. Pencer, …, J. Katsaras. 2007. Curvature effect on the structure of phospholipid bilayers. *Langmuir.* 23:1292–1299.
42. Kucerka, N., M. P. Nieh, and J. Katsaras. 2009. Asymmetric distribution of cholesterol in unilamellar vesicles of monounsaturated phospholipids. *Langmuir.* 25:13522–13527.
43. Szekely, O., A. Steiner, …, U. Raviv. 2011. The structure of ions and zwitterionic lipids regulates the charge of dipolar membranes. *Langmuir.* 27:7419–7438.
44. Alsop, R. J., R. Maria Schober, and M. C. Rheinstädter. 2016. Swelling of phospholipid membranes by divalent metal ions depends on the location of the ions in the bilayers. *Soft Matter.* 12:6737–6748.
45. Lotan, O., L. Fink, …, U. Raviv. 2016. Critical conditions for adsorption of calcium ions onto dipolar lipid membranes. *J. Phys. Chem. A.* 120:3390–3396.
46. Castorph, S., L. Arleth, …, T. Salditt. 2010. Synaptic vesicles studied by SAXS: derivation and validation of a model form factor. *J. Phys. Conf. Ser.* 247:012015.

**Biophysical Journal, Volume *114***

## Supplemental Information

# Vesicle Adhesion and Fusion Studied by Small-Angle X-Ray Scattering

**Karlo Komorowski, Annalena Salditt, Yihui Xu, Halenur Yavuz, Martha Brennich, Reinhard Jahn, and Tim Salditt**

# 1 Dynamic Light Scattering

Dynamic light scattering (DLS) measurements were performed by using an ALV/CGS-3 DLS/SLS Laser Light Scattering Goniometer System (ALV GmbH Langen, Germany). The setup is equipped with a 22 mW polarized HeNe-Laser operating at a wavelength of $\lambda = 632.8$ nm (UNIPHASE, model 1145P), and an ALV-7004 Multiple Tau Digital Correlator. Scattering intensities were recorded using an ALV high quantum efficiency avalanche diode at a scattering angle of 90°. Cylindrical borosilicate cuvettes with a diameter of 10 mm (Fisher Scientific), closed with polymer caps (Carl Roth GmbH, Karlsruhe, Germany), were used as sample cells. For matching the refractive index of the cuvettes the measurement cell in the setup was filled with toluene. In all experiments the samples were diluted 1 : 500 with Milli-Q water, which was additionally filtered through a membrane of 20 nm pore size. For each sample, three runs of ten seconds were performed to calculate the intensity correlation functions. These correlation functions were than averaged to obtain the averaged intensity autocorrelation function $g_2(\tau) = \langle I(t)I(t+\tau)\rangle_t / \langle I\rangle_t^2$, which is related to the resulting normalized amplitude correlation function $g_1(\tau)$ by the Siegert relation $g_2(\tau) = 1 + \beta|g_1(\tau)|^2$ with the coherence factor $\beta$. Data analysis was performed with the ALV-Correlator Software (ALV-7004 for Windows, V.3.0.5.4) using a constrained regularization method for applying nonlinear fits to $\beta|g_1(\tau)|^2$. Fig. S1 shows size distributions of vesicles obtained by DLS for different lipid compositions with respect to the preparation step. DLS measurements were performed directly after the respective preparation step involving sonication in the first step and subsequently serial extrusion through polycarbonate membranes with pore sizes of 100, 50 and 30 nm diameter, in this order. In general, we observe that the extrusion steps affect the structure of the vesicles for both parameters, the mean radius and the polydispersity of the vesicle suspension, compared to sonicated vesicles. Both parameters are generally slightly decreased after each extrusion step. Only for DOPS huge differences can be observed for the polydispersity. Nevertheless, direct sonication of the suspension already leads to comparatively small vesicles. Note that DLS is particularly sensitive to contamination by larger aggregates, and size distribution are often 'corrected' by weighting functions, see for example (1). Here we show only unweighted distributions.

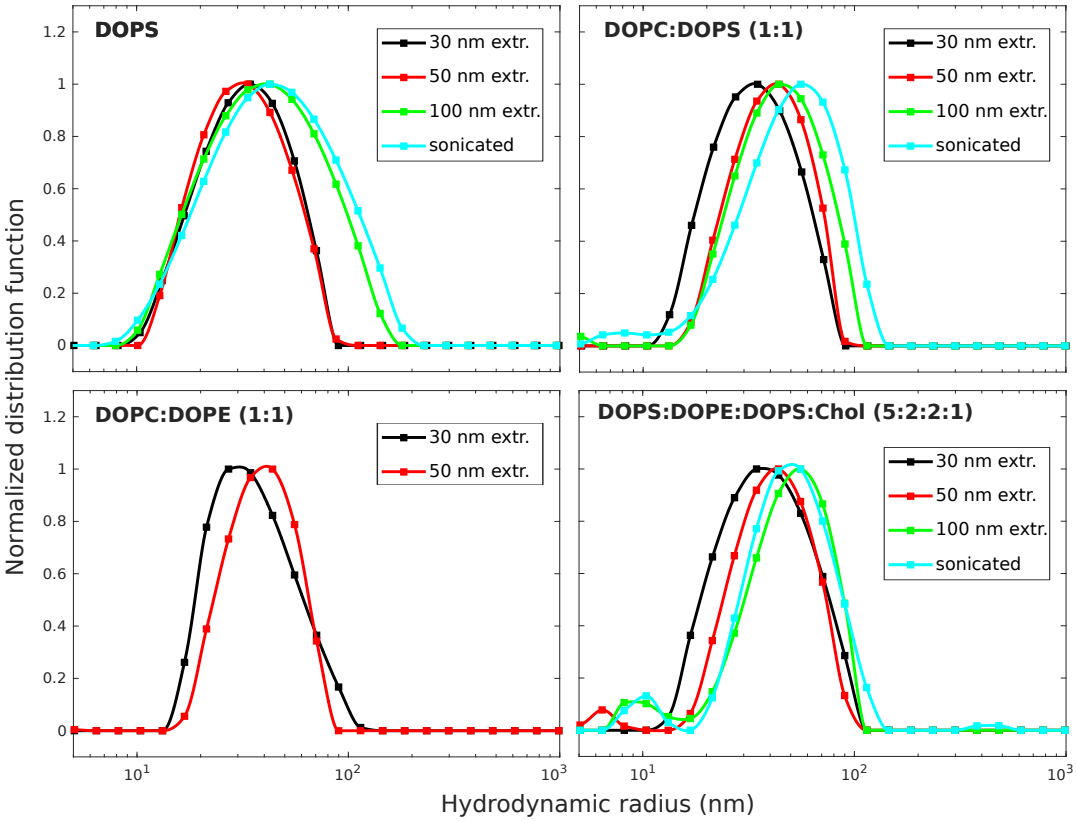


**Fig. S1:** Size distributions of lipid vesicles obtained by DLS for different lipid compositions with respect to the preparation step. The vesicles were first sonicated, then extruded through polycarbonate membranes with pore sizes of 100 nm, 50 nm, and 30 nm, in this order.

## 2 Non-interacting vesicles: additional figures and tables

Fig. S2 shows a series of SAXS profiles $I(q)$ vs $q$ of vesicles in ultra-pure water for different lipid compositions. The measurements were performed immediately after the respective

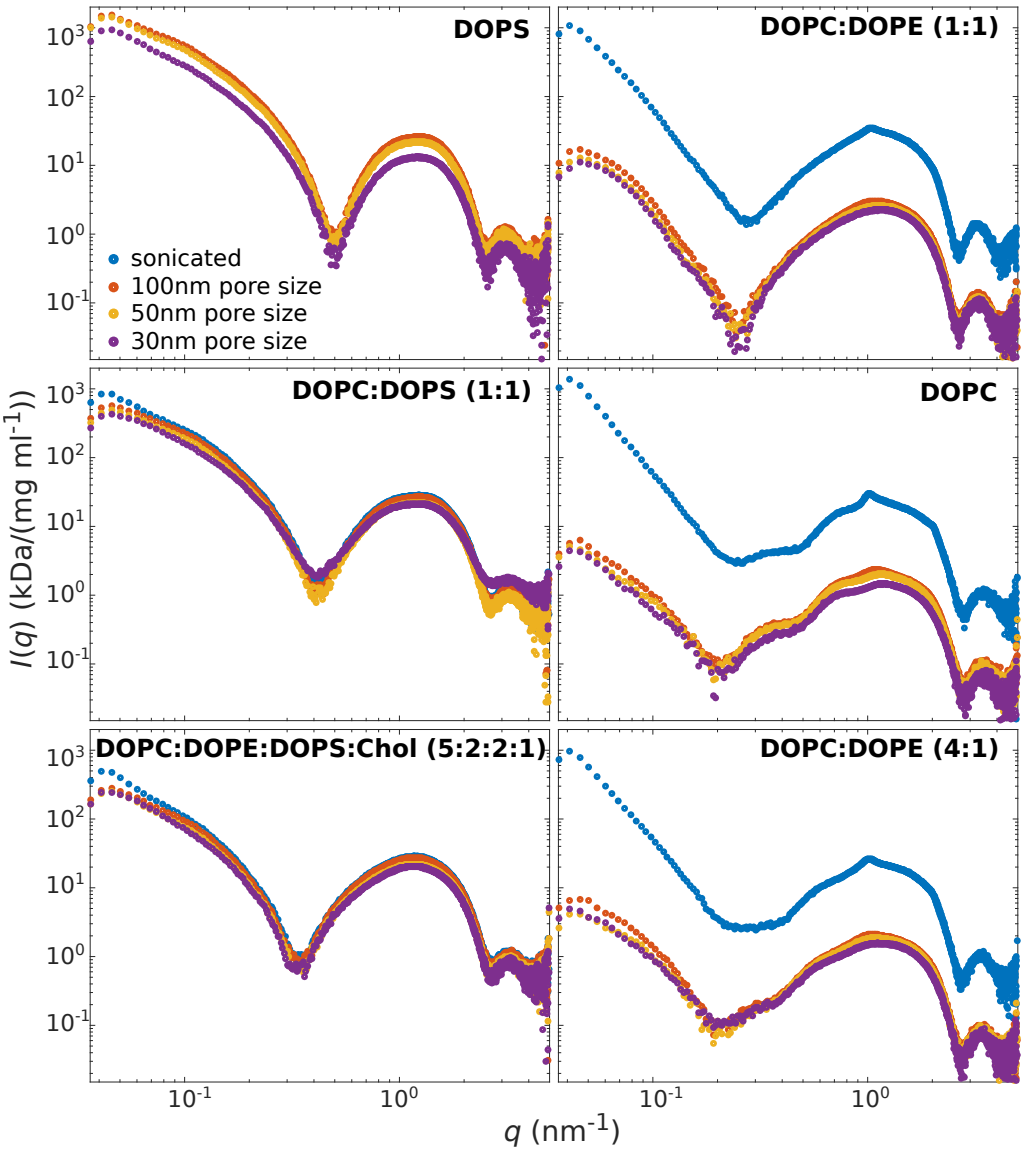


**Fig. S2:** SAXS data $I(q)$ vs. $q$ for vesicles of different composition and preparation steps in ultra-pure water. The vesicles were first sonicated (blue circles), then gradually extruded through polycarbonate membranes with pore sizes of 100 nm (red circles), 50 nm (yellow circles), 30 nm (purple circles), in this order.

preparation step (subsequent extrusion through membranes of 100 nm, 50 nm and 30 nm pore size). As already discussed in the main text, we observe that vesicles containing DOPS achieve unilamellarity easily for each data set. Contrary, unilamellar vesicle using DOPC:DOPE mixtures are only achieved for DOPC:DOPE (1:1) after the final step of

extrusion through 30 nm pores.
Next, we present additional fits of non-interacting vesicles without proteins, and focus in particular on the influence of different background models. Note that the workflow always included background subtraction in form of a pure buffer measurement. However, residual errors occur if this subtraction is not completely correct for example by issues of self absorption. This can be accounted for by an additional parameterized background model (additive with either sign).

**Spherical vesicle model fits with different background models.** Fig. S3 shows SAXS data of (a) DOPC:DOPE (1:1)-vesicles and (b) DOPS-vesicles (black circles) as well as least-squares fits based on the spherical vesicle model (blue lines) assuming a symmetric bilayer profile. The subplots show least-squares fits for different background models: (top) Without a background model, (center) with an additional constant background model and (bottom) with an additional power-law background model (orange lines). The structural parameters and the $\chi^2_{\mathrm{red}}$-values obtained from the least-squares fits are summarized in Tab. S1,S2,S3.
If no background model was added to the spherical vesicle model, we observe discrepancies between the least-squares fits and the SAXS data in particular for the form factor minima. In the case of a constant background model, a good match can be observed for higher $q$-values, whereas discrepancies still appear in the lower $q$-region. The discrepancies are most pronounced for DOPC:DOPE vesicles. For DOPS vesicles the differences are less obvious, but at a closer look we observe modulations of the least-squares fit in the very low $q$-range which do not match with the experimental data. Using a power-law background model, we observe a good match between the least-squares fits and the data over the entire $q$-range. Consequently, the $\chi^2_{\mathrm{red}}$-values are reduced. The comparison of the two power-law backgrounds (Fig. S3, bottom) indicates that the background depends on the lipid composition of the vesicles. We conclude that the background model describes discrepancies between the SAXS data and the spherical vesicle model rather than a real effect of flawed experimental background, for example, due to deviations from a spherical structure. In the following we investigate how structural parameters depend on the background model.

**Structural results for each data set, a model-based discussion.** Fig. S4 displays the structural parameters for each lipid composition along with the corresponding preparation step as obtained from the least-squares analysis using the flat bilayer model with an additional constant background (blue circles), or the spherical vesicle model with either an additional constant background (green circles) or a power-law background model (red circles). The structural parameters as well as the $\chi^2_{\mathrm{red}}$-values can be further

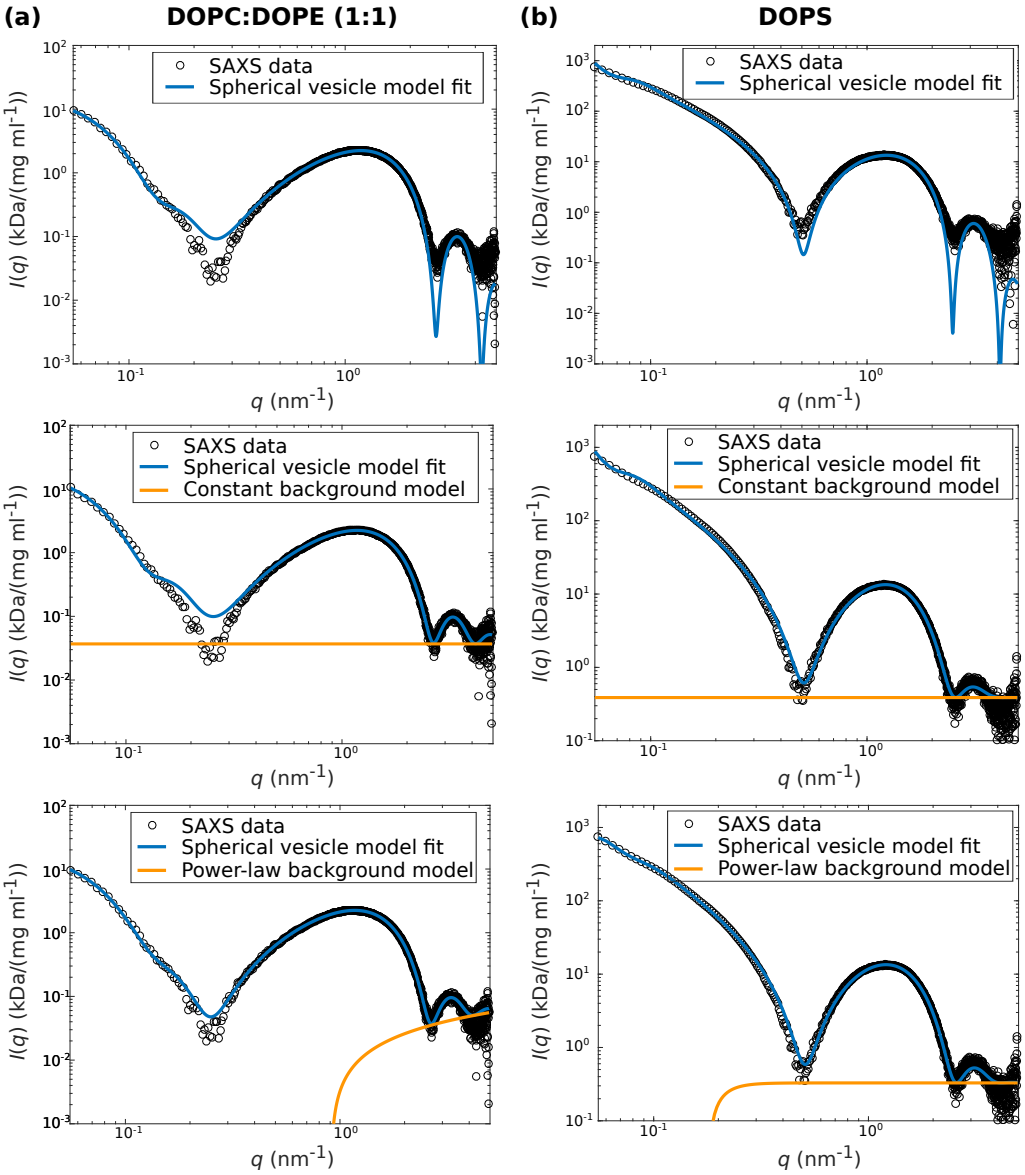


**Fig. S3:** Comparison of different background models (orange lines) for (a) 30nm extruded DOPC:DOPE (1:1)-vesicles and (b) 30 nm extruded DOPS-vesicles (black circles). Analysis includes spherical vesicle model least-squares fits (blue lines) without a background model (top), with a constant background model (center) and with a power-law background model (bottom).

found in the Tab. S1 (flat bilayer model, constant background), S3 (spherical vesicle model analysis, constant background) and S2 (spherical vesicle model analysis, power-law background). The four upper plots display the obtained bilayer parameters $\sigma_{\mathrm{h}}$, $\sigma_{\mathrm{c}}$, $\rho_{\mathrm{h}}$ and $d_{\mathrm{hh}}$, while the two lower plots show the vesicle parameters $R_0$ and $\sigma_{\mathrm{R}}$. In the case of the spherical vesicle model analysis, we observe that the obtained structural parameters depend on the underlying background model. The dependence is less pronounced for the bilayer parameters, but strong for the mean radii. By visual inspection (cf. Fig. S3), the spherical vesicle model with a constant background was not able to match the data in the lower $q$-region.

Comparing the results of the spherical vesicle model analysis to those of the flat bilayer model analysis, we observe that the structural bilayer parameters obtained from the flat bilayer model are systematically closer to those of the spherical vesicle model using an additional power-law background. This observation indicates that the results obtained from the spherical vesicle model with a power-law background are reasonable at least for the bilayer parameters. Still for the spherical vesicle model with a power-law background, major changes in the radius occur between vesicles extruded through 50 nm pore sizes and through 30 nm pore sizes. DOPC:DOPE (1:1)-vesicles are an exception, since for both preparation steps a radius of approximately 14 nm is obtained. Simultaneously, DOPC:DOPE (1:1)-vesicles show the smallest radius as compared to the other lipid compositions. One explanation for no or only minor changes in the radius between the preparation steps sonication and extrusion through pores of 50 nm diameter could be that already the sonication step leads to small mean radii. The mean radii obtained from the spherical vesicle model analysis with an additional constant background are significantly higher for each lipid composition. Unexpectedly, the mean radius shows an increase from the sonication step to the step of extrusion through 100 nm pores for DOPC:DOPS (1:1) and DOPC:DOPE:DOPS:Chol (5:2:2:1).

Nevertheless, independently of the background model we observe the smallest radii for DOPC:DOPE (1:1) vesicles ($\sim$ 14 to 18 nm). This observation is well in line with the fact that contrary to the other lipid compositions the net charge of the mixture is zero. Thus, there is no long-range repulsion due to a negatively charged surface. The values for the standard deviation $\sigma_{\mathrm{R}}$ of the size distribution of the vesicle suspension appear to be high with respect to the corresponding mean radius (for almost each lipid composition approximately $\sigma_{\mathrm{R}}/R_0 = 0.5$). The lowest values for $\sigma_{\mathrm{R}}$ can be found for DOPC:DOPE (1:1) vesicles.

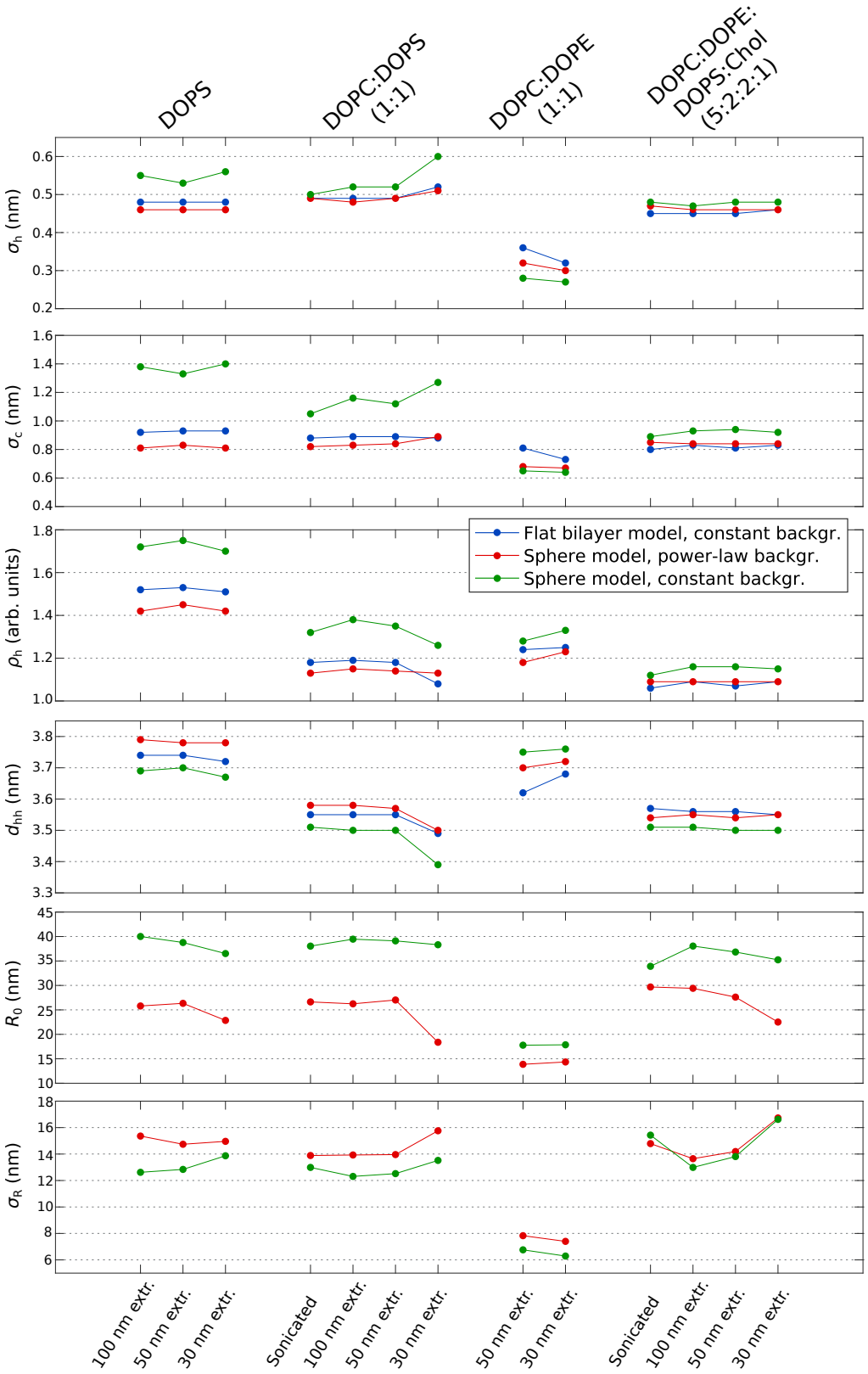


**Fig. S4:** Structural parameters obtained from least-squares fits using the flat bilayer model and the spherical vesicle model with different background models for 13 data sets (four different lipid compositions and up to four different preparation steps).

| Lipid composition | Preparation | $\rho_{\mathrm{h}}$ (arb. u.) | $\sigma_{\mathrm{h}}$, $\sigma_{\mathrm{c}}$ (nm) | $d_{\mathrm{hh}}$ (nm) | $\chi^2_{red}$ | $c_1$ | $c_2$ |
|---|---|---|---|---|---|---|---|
| DOPS | 100 nm extr. | 1.52 | 0.48, 0.92 | 3.74 | 5.19 | 23.34 | 0.64 |
| | 50 nm extr. | 1.53 | 0.48, 0.93 | 3.74 | 3.66 | 19.66 | 0.57 |
| | 30 nm extr. | 1.51 | 0.48, 0.93 | 3.72 | 2.30 | 11.92 | 0.35 |
| DOPC:DOPS (1:1) | sonicated | 1.18 | 0.49, 0.88 | 3.55 | 4.95 | 38.90 | 0.89 |
| | 100 nm extr. | 1.19 | 0.49, 0.89 | 3.55 | 3.57 | 36.24 | 0.82 |
| | 50 nm extr. | 1.18 | 0.49, 0.89 | 3.55 | 2.67 | 30.36 | 0.68 |
| | 30 nm extr. | 1.08 | 0.52, 0.88 | 3.49 | 3.94 | 31.31 | 1.45 |
| DOPC:DOPE (1:1) | 50 nm extr. | 1.24 | 0.36, 0.81 | 3.62 | 2.79 | 3.87 | 0.05 |
| | 30 nm extr. | 1.26 | 0.32, 0.73 | 3.68 | 1.15 | 3.56 | 0.04 |
| DOPC:DOPE:DOPS:Chol (5:2:2:1) | sonicated | 1.06 | 0.45, 0.80 | 3.57 | 2.00 | 43.47 | 0.78 |
| | 100 nm extr. | 1.09 | 0.45, 0.83 | 3.56 | 1.73 | 40.79 | 0.73 |
| | 50 nm extr. | 1.07 | 0.45, 0.81 | 3.56 | 1.72 | 33.57 | 0.61 |
| | 30 nm extr. | 1.09 | 0.46, 0.83 | 3.55 | 1.73 | 30.88 | 0.55 |

**Tab. S1:** Structural parameters obtained from flat bilayer model fits to SAXS data of various lipid compositions with respect to the preparation (sonicated and extruded through polycarbonate membranes with pore sizes 100 nm, 50 nm and 30 nm in diameter). The model fits are based on a symmetric electron density profile, thus the amplitude and width of the inner and outer leaflet are $\rho_{\mathrm{h}} = \rho_{\mathrm{h1}} = \rho_{\mathrm{h2}}$ and $\sigma_{\mathrm{h}} = \sigma_{\mathrm{h1}} = \sigma_{\mathrm{h2}}$. The amplitude of the Gaussian representing the chain region is selected to $\rho_c = -1$ (arb. units) for all fits.

| Lipid composition | Preparation | $\rho_{\mathrm{h}}$ (arb. u.) | $\sigma_{\mathrm{h}}$, $\sigma_{\mathrm{c}}$ (nm) | $d_{\mathrm{hh}}$ (nm) | $R_0$ (nm) | $\sigma_R$ (nm) | $\chi^2_{red}$ | $c_1$ | $c_2$ | $c_3$ | $c_4$ |
|---|---|---|---|---|---|---|---|---|---|---|---|
| DOPS | 100 nm extr. | 1.42 | 0.46, 0.81 | 3.79 | 25.8 | 15.36 | 9.14 | 0.014 | $-7.42 \cdot 10^{-6}$ | 6.52 | 0.61 |
| | 50 nm extr. | 1.45 | 0.46, 0.83 | 3.78 | 26.34 | 14.74 | 5.92 | 0.011 | $-2.93 \cdot 10^{-6}$ | 6.77 | 0.54 |
| | 30 nm extr. | 1.42 | 0.47, 0.81 | 3.78 | 22.85 | 14.96 | 3.77 | 0.008 | $-5.15 \cdot 10^{-6}$ | 6.42 | 0.33 |
| DOPC:DOPS (1:1) | sonicated | 1.13 | 0.49, 0.82 | 3.58 | 26.63 | 13.89 | 7.56 | 0.022 | $-2.54 \cdot 10^{-7}$ | 7.43 | 0.86 |
| | 100 nm extr. | 1.15 | 0.48, 0.83 | 3.58 | 26.24 | 13.93 | 5.61 | 0.021 | $-1.36 \cdot 10^{-6}$ | 6.88 | 0.79 |
| | 50 nm extr. | 1.14 | 0.49, 0.84 | 3.57 | 27.02 | 13.96 | 3.63 | 0.017 | $-3.24 \cdot 10^{-7}$ | 7.28 | 0.65 |
| | 30 nm extr. | 1.13 | 0.51, 0.89 | 3.5 | 18.38 | 15.76 | 3.79 | 0.026 | $-2.52 \cdot 10^{-5}$ | 5.8 | 1.41 |
| DOPC:DOPE (1:1) | 50 nm extr. | 1.18 | 0.32, 0.68 | 3.7 | 13.87 | 7.83 | 3.34 | 0.009 | 1010.85 | $-3.97 \cdot 10^{-5}$ | -1010.85 |
| | 30 nm extr. | 1.23 | 0.3, 0.67 | 3.72 | 14.35 | 7.4 | 1.42 | 0.007 | 808.51 | $-4.05 \cdot 10^{-5}$ | -808.51 |
| DOPC:DOPE:DOPS:Chol (5:2:2:1) | sonicated | 1.09 | 0.47, 0.85 | 3.54 | 29.68 | 14.79 | 3.05 | 0.021 | $-3.04 \cdot 10^{-12}$ | 10.77 | 0.76 |
| | 100 nm extr. | 1.09 | 0.46, 0.84 | 3.55 | 29.41 | 13.65 | 2.47 | 0.020 | $-9.71 \cdot 10^{-10}$ | 8.96 | 0.71 |
| | 50 nm extr. | 1.09 | 0.46, 0.84 | 3.54 | 27.61 | 14.19 | 2.1 | 0.018 | $-8.22 \cdot 10^{-10}$ | 8.93 | 0.59 |
| | 30 nm extr. | 1.09 | 0.46, 0.84 | 3.55 | 22.51 | 16.73 | 2.08 | 0.019 | $-1.97 \cdot 10^{-10}$ | 9.34 | 0.53 |

**Tab. S2:** Structural parameters obtained from spherical vesicle model fits $I_{\mathrm{tot}}(q) = c_1 I_{\mathrm{sphere}}(q) + c_2 q^{-c_3} + c_4$ to SAXS data of various lipid compositions with respect to the preparation (sonicated and extruded through polycarbonate membranes with pore sizes 100 nm, 50 nm and 30 nm in diameter). The model fits are based on a symmetric electron density profile, thus the amplitude and width of the inner and outer leaflet are $\rho_{\mathrm{h}} = \rho_{\mathrm{h1}} = \rho_{\mathrm{h2}}$ and $\sigma_{\mathrm{h}} = \sigma_{\mathrm{h1}} = \sigma_{\mathrm{h2}}$. The amplitude of the Gaussian representing the chain region is selected to $\rho_c = -1$ (arb. units) for all fits.

| Lipid composition | Preparation | $\rho_{\mathrm{h}}$ (arb. u.) | $\sigma_{\mathrm{h}}$, $\sigma_{\mathrm{c}}$ (nm) | $d_{\mathrm{hh}}$ nm) | $R_0$ (nm) | $\sigma_R$ (nm) | $\chi^2_{red}$ | $c_1$ | $c_2$ |
|---|---|---|---|---|---|---|---|---|---|
| DOPS | 100 nm extr. | 1.72 | 0.55, 1.38 | 3.69 | 40.01 | 12.62 | 58.38 | 0.004 | 0.39 |
| | 50 nm extr. | 1.75 | 0.53, 1.33 | 3.70 | 38.78 | 12.84 | 34.58 | 0.006 | 0.60 |
| | 30 nm extr. | 1.70 | 0.56, 1.40 | 3.67 | 36.52 | 13.87 | 21.58 | 0.007 | 0.71 |
| DOPC:DOPS (1:1) | sonicated | 1.32 | 0.50, 1.05 | 3.51 | 38.04 | 12.99 | 22.37 | 0.012 | 0.88 |
| | 100 nm extr. | 1.38 | 0.52, 1.16 | 3.50 | 39.46 | 12.31 | 26.72 | 0.010 | 0.84 |
| | 50 nm extr. | 1.35 | 0.52, 1.12 | 3.50 | 39.11 | 12.52 | 15.89 | 0.009 | 0.68 |
| | 30 nm extr. | 1.26 | 0.60, 1.27 | 3.39 | 38.32 | 13.52 | 15.25 | 0.011 | 1.48 |
| DOPC:DOPE (1:1) | 50 nm extr. | 1.28 | 0.28, 0.65 | 3.75 | 17.78 | 6.76 | 4.89 | 0.006 | 0.04 |
| | 30 nm extr. | 1.33 | 0.27, 0.64 | 3.76 | 17.86 | 6.29 | 2.39 | 0.005 | 0.04 |
| DOPC:DOPE:DOPS:Chol (5:2:2:1) | sonicated | 1.12 | 0.48, 0.89 | 3.51 | 33.91 | 15.43 | 3.42 | 0.015 | 0.77 |
| | 100 nm extr. | 1.16 | 0.47, 0.93 | 3.51 | 38.05 | 12.99 | 4.65 | 0.012 | 0.72 |
| | 50 nm extr. | 1.16 | 0.48, 0.94 | 3.50 | 36.83 | 13.81 | 3.44 | 0.010 | 0.60 |
| | 30 nm extr. | 1.15 | 0.48, 0.92 | 3.50 | 35.24 | 16.62 | 2.52 | 0.010 | 0.54 |

**Tab. S3:** Constant Background. Structural parameters obtained from spherical vesicle model fits to SAXS data of various lipid compositions with respect to the preparation (sonicated and extruded through polycarbonate membranes with pore sizes 100 nm, 50 nm and 30 nm in diameter). The model fits are based on a symmetric electron density profile, thus the amplitude and width of the inner and outer leaflet are $\rho_{\mathrm{h}} = \rho_{\mathrm{h1}} = \rho_{\mathrm{h2}}$ and $\sigma_{\mathrm{h}} = \sigma_{\mathrm{h1}} = \sigma_{\mathrm{h2}}$. The amplitude of the Gaussian representing the chain region is selected to $\rho_c = -1$ (arb. units) for all fits.

## 3 Adhesion of vesicles: additional figures and tables

Based on the analysis of the SAXS data of $CaCl_2$- and $MgCl_2$-induced adhesion of lipid vesicles presented in the main manuscript (Fig. 5, Tab. 2), we further compare the EDPs upon addition of the divalent ions and of the control (without divalent ions) in Fig. S5. Both for $CaCl_2$ and $MgCl_2$ a swelling of the lipid bilayer is observed. Subtraction of the EDPs ($\rho_{CaCl_2} - \rho_{control}$ and $\rho_{MgCl_2} - \rho_{control}$) gives pronounced peaks close to the headgroup maxima (identified as the phosphorus), revealing the position of the condensated $Ca^{2+}$ and $Mg^{2+}$ ions. Accordingly, the ions are located near the bilayer surface with a rather small penetration depth into the headgroup region (the insertion is less for $Ca^{2+}$).

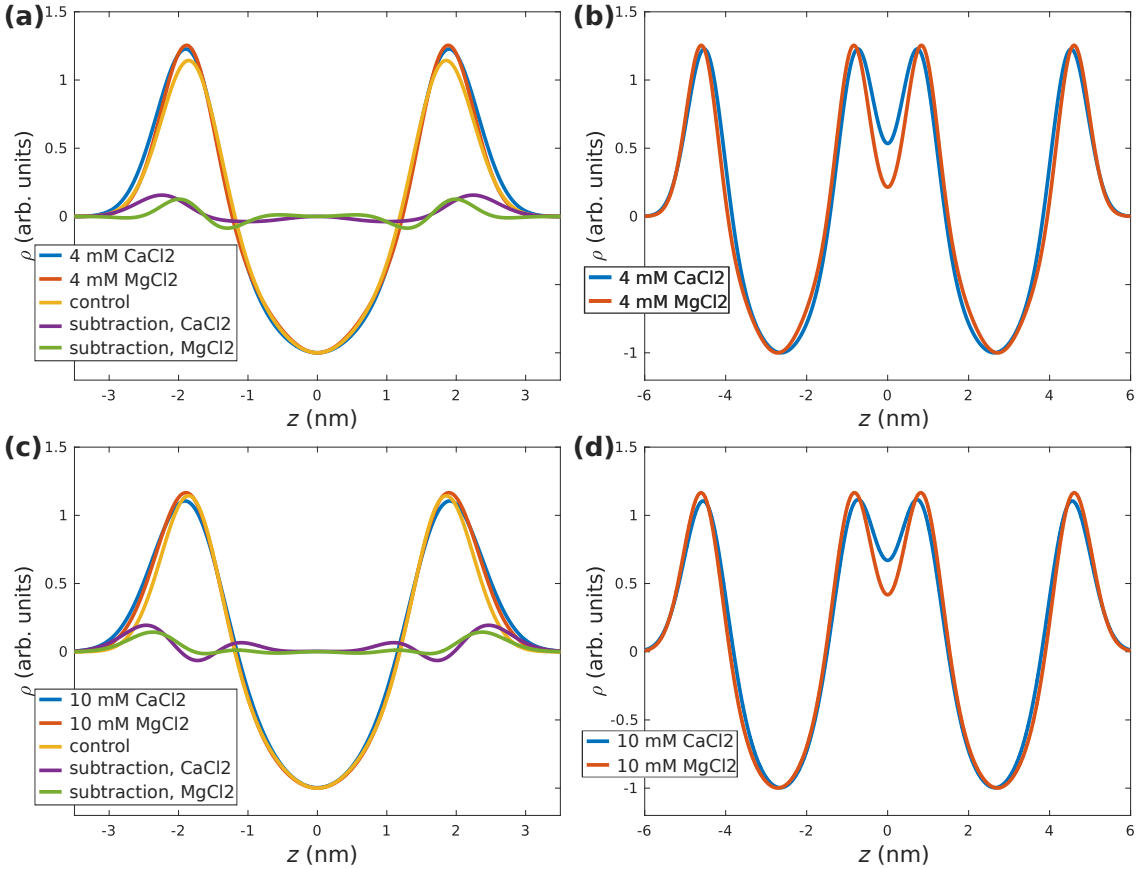


**Fig. S5:** Reconstructed EDPs of DOPC:DOPS (1:1) with (a,b) 4 mM $CaCl_2$/$MgCl_2$ and (c,d) 10 mM $CaCl_2$/$MgCl_2$ using the structural parameters obtained from the flat bilayer model fits and from the docking model fits presented in the main manuscript in Fig. 5 and Tab. 2. The EDPs indicated as control correspond to the flat bilayer analysis of the SAXS data without added salts.

Next, we present data obtained in a soft adhesion regime with inter-bilayer water distances much larger than for the strong adhesion regime described in the main manuscript. This regime is observed when the addition of $CaCl_2$ is accompanied by monovalent salt (KCl).

For the recording of that data, we have used $CaCl_2$ in a HEPES buffer (10mM $CaCl_2$, 150mM KCl and 20mM Hepes, pH 7.4). Fig. S6 shows the corresponding series of SAXS curves $I(q)$ vs. $q$ of vesicles initially suspended in ultra-pure water, as a function of the added $CaCl_2$ and KCl concentration. The SAXS profiles of the DOPC:DOPS (1:1) mixture

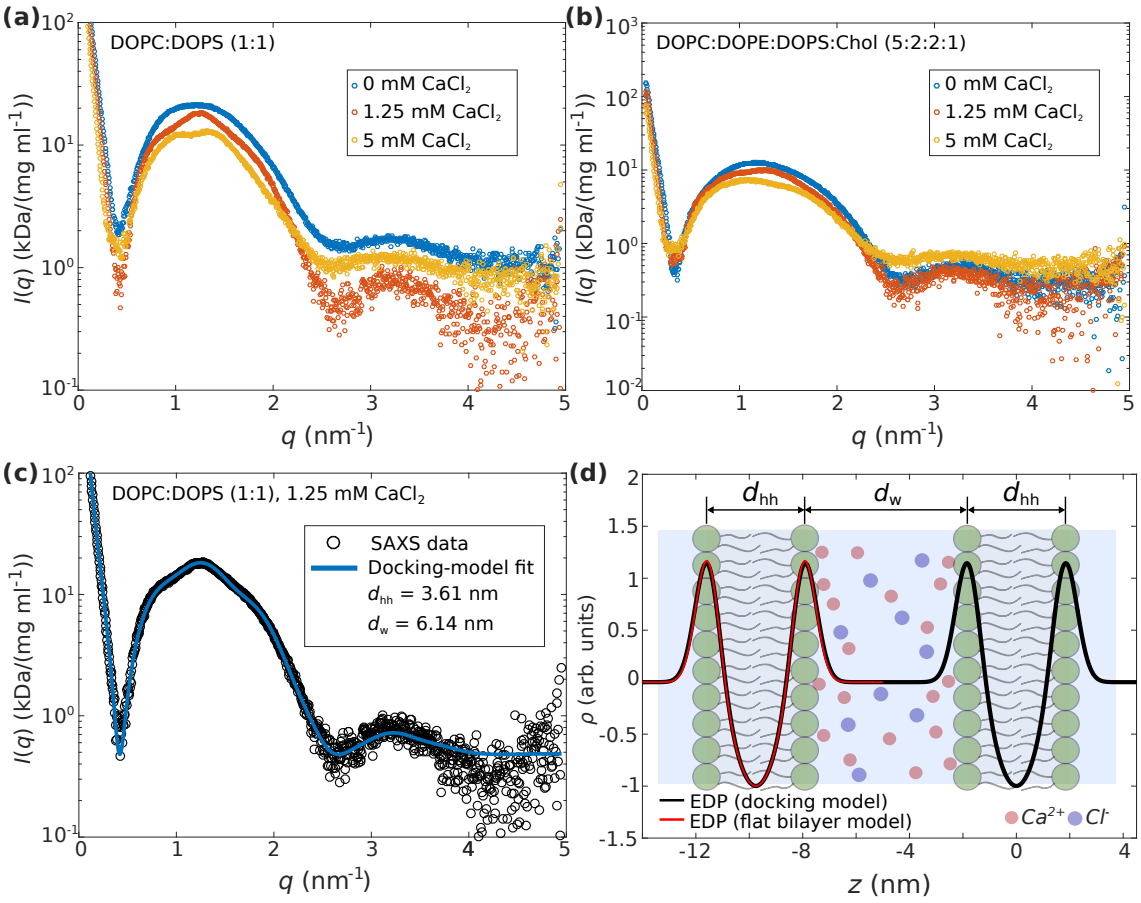


**Fig. S6:** (a) SAXS data of DOPC:DOPS (1:1) vesicles in Milli-Q water with added $CaCl_2$ with concentrations of 0 mM (blue), 1.25 mM (red) and 5 mM (yellow). (b) SAXS data of DOPC:DOPE:DOPS:Chol (5:2:2:1) vesicles in Milli-Q water with added $CaCl_2$ with concentrations of 0 mM (blue), 1.25 mM (red) and 5 mM (yellow). (c) Scattering curve as obtained from DOPC:DOPS (1:1) vesicles in Milli-Q water upon addition of 1.25 mM $CaCl_2$ (black circles) and least-squares fit using the docking model (blue line). (d) EDP as obtained from the docking model fit indicated in (c). The structural parameters are summarized in Tab. S4.

(a) and the DOPC:DOPE:DOPS:Chol (5:2:2:1) mixture (b) show the characteristic structure factor modulations of two membranes in an adhering state. The modulation varying systematically with ion concentrations, indicating that the range of water layer spacings is much more variable than in the strong adhesion regime. As an example, we explicitly show in (c) the analysis of the SAXS data of DOPC:DOPS (1:1) vesicles in the presence of 1.25 mM $CaCl_2$ and 18.75 mM KCl, based on the docking model with a constant background

model. The structural parameters obtained from the least-squares fits to the docking model are listed in Tab. S4 for each data set. In (d), the corresponding EDP of the two docked bilayers is displayed (black line). Next to the structural bilayer parameters, the interbilayer spacing (or water spacing) is quantified in a robust manner, yielding $d_{\mathrm{w}} = 6.14$ nm. Furthermore, the EDP of unilamellar DOPC:DOPS (1:1) vesicles as obtained from the flat bilayer model fit (supplementary information, Tab. 1) is indicated (red line). In this example, the bilayer structure exhibits only minor changes due to the addition of $CaCl_2$. As is apparent from Tab. S4, the water spacing is decreased for an increased $CaCl_2$ concentration ($d_{\mathrm{w}} = 3.79$ nm in the case of 5 mM $CaCl_2$). For the more complex lipid mixture of DOPC:DOPE:DOPS:Chol (5:2:2:1), a similar trend can be observed. While the water spacing of $d_{\mathrm{w}} = 5.48$ nm is again rather high for 1.25 mM $CaCl_2$, a decreased water spacing of $d_{\mathrm{w}} = 3.03$ was obtained for 5 mM $CaCl_2$. Interestingly, comparing the values for $d_{\mathrm{w}}$ between the different lipid compositions at the same $CaCl_2$ concentration, we can see that the water spacing is always smaller for DOPC:DOPE:DOPS:Chol (5:2:2:1). This observation may result from the lower surface charge density $\sigma$ in the 4-component mixture (20 mol% DOPS).

In summary, we observe the following: (1) An increase of the $CaCl_2$ and KCl concentration yields a decrease of the interbilayer spacing $d_{\mathrm{w}}$ and (2) an increase of $\sigma$ at constant ion concentrations yields an increase of $d_{\mathrm{w}}$.

| Lipid composition | $[CaCl_2]$ (mM) | [KCl] (mM) | $\rho_{\mathrm{h}}$ (a. u.) | $\sigma_{\mathrm{h}}$, $\sigma_{\mathrm{c}}$ (nm) | $d_{\mathrm{hh}}$ (nm) | $d_{\mathrm{w}}$ (nm) | $(1-\nu_{\mathrm{d}})$ | $\chi^2_{red}$ |
|---|---|---|---|---|---|---|---|---|
| DOPC:DOPS (1:1) | 1.25 | 18.75 | 1.27 | 0.46, 089 | 3.61 | 6.14 | 0.96 | 1.7 |
| | 5 | 75 | 1.32 | 0.38, 0.75 | 3.79 | 4.82 | 0.97 | 2.2 |
| DOPC:DOPE:DOPS:Chol (5:2:2:1) | 1.25 | 18.75 | 1.09 | 0.46, 0.85 | 3.6 | 5.48 | 0.98 | 2.26 |
| | 5 | 75 | 1.02 | 0.47, 0.83 | 3.58 | 3.69 | 0.97 | 1.39 |

**Tab. S4:** Structural parameters as obtained from docking model fits to SAXS data of docked DOPC:DOPS (1:1) and DOPC:DOPE:DOPS:Chol (5:2:2:1) vesicles with respect to the $CaCl_2$ concentration. The model fits are based on a symmetric EDP, thus the amplitude and width of the inner and outer leaflet are $\rho_{\mathrm{h}} = \rho_{\mathrm{h1}} = \rho_{\mathrm{h2}}$ and $\sigma_{\mathrm{h}} = \sigma_{\mathrm{h1}} = \sigma_{\mathrm{h2}}$. The amplitude of the Gaussian representing the chain region is selected to $\rho_c = -1$ for all fits.

# 4 SNARE-mediated liposome fusion and docking experiments

To study SNARE-mediated liposome fusion intermediates, two types of experiments were performed. For the docking and fusion experiments liposomes reconstituted with either the mutant SybΔ84, or with SybWT, respectively, were used. For both experiments liposomes reconstituted with the ΔN complex as the acceptor complex were used. Fusion is distinctly inhibited by using the SybΔ84 mutant (2).

In (a) and (b) the SAXS curves $I(q)$ vs. $q$ are shown for the fusion experiment (mixed SybWT- and ΔN-liposomes at a molar ratio of 1:1) and the docking experiments (mixed SybΔ84- and ΔN-liposomes at a molar ratio of 1:1), respectively. Furthermore, the SAXS data of the docking and fusion experiments are compared to the mean scattering of the individual SNARE-liposomes. The mean scattering curve would be the expected scattering curve if no reaction occurred upon mixing. Then the scattering intensity is the incoherent superposition $I(q) = (I_{\mathrm{A}}(q) + I_{\mathrm{B}}(q))/2$ of the two individual contributions. The factor $1/2$ accounts for the dilution of each individual SNARE-liposome population. By comparison of the mean scattering curves and the scattering curves from the docking and fusion experiments, we observe small but systematic differences in the low $q$-region, and a slight increase of the scattering intensity over the entire $q$-region.

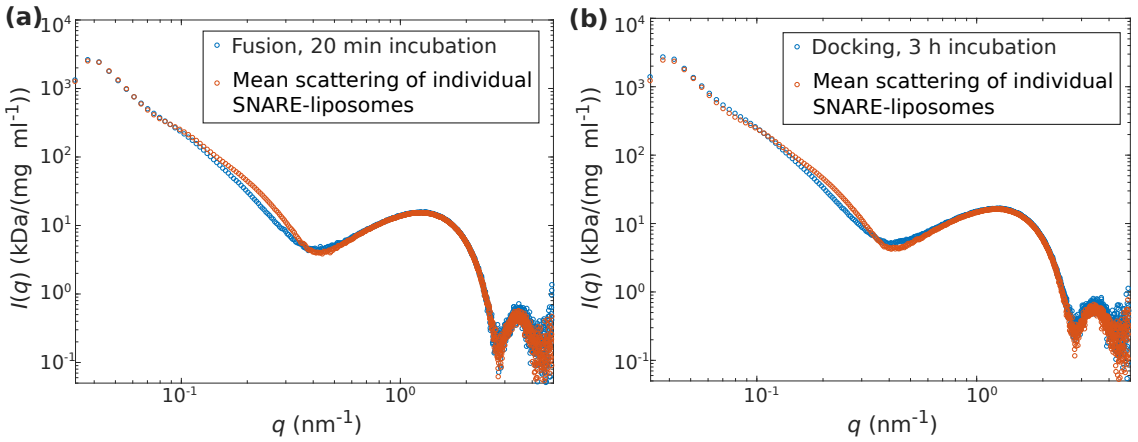


**Fig. S7:** (a) and (b) show SAXS data of SNARE-mediated fusion (mixed SybWT- and ΔN-liposomes) and docking (mixed SybΔ84- and ΔN-liposomes) experiments compared to the calculated mean scattering curves $(I_{\mathrm{SybWT}}(q) + I_{\Delta\mathrm{N}}(q))/2$ in the case of the fusion experiments and $(I_{\mathrm{SybΔ84}}(q) + I_{\Delta\mathrm{N}}(q))/2$ in the case of the docking experiment

In the case of the docking experiments, the characteristic structure factor modulations observed in the calcium-induced vesicle adhesion are not observed. Therefore, it is not possible to analyze the SAXS data by least-squares fits using the docking model to obtain the water spacing $d_{\mathrm{w}}$. We conclude that the signal of the docking and fusion states may

have been lost in the ensemble average of the SAXS experiment, i.e.that docking and fusion efficiencies have been insufficient. This conclusion is supported by the following estimate of the increase of the forward scattering intensity, made for the case of 100 % fusion efficiency, we consider a form factor model of a spherical shell. The scattering intensity $I_{\mathrm{shell}}(q)$ is given by (3)

$$\begin{aligned} I_{shell}(q) &= \Delta\rho^2 V_{\mathrm{shell}}^2 |f_{\mathrm{shell}}(q)|^2 \\ &= \Delta\rho^2 V_{\mathrm{shell}}^2 \left| \frac{V(R_{\mathrm{out}}) f_{\mathrm{sphere}}(q, R_{\mathrm{out}}) - V(R_{\mathrm{in}}) f_{\mathrm{sphere}}(q, R_{\mathrm{in}})}{V(R_{\mathrm{out}}) - V(R_{\mathrm{in}})} \right|^2 , \end{aligned} \tag{1}$$

where

$$f_{\mathrm{sphere}}(q, R) = \frac{3(\sin(qR) - qR\cos(qR))}{(qR)^3} \tag{2}$$

is the form factor of a homogeneous sphere, $V(R) = 4/3\pi R^3$ is the volume of a sphere with the radius $R$, and $V_{\mathrm{shell}} = 4/3\pi(R_{\mathrm{out}}^3 - R_{\mathrm{in}}^3)$ is the volume of the shell with the outer and inner radius $R_{\mathrm{out}}$ and $R_{\mathrm{in}}$, respectively. For the forward scattering intensity $q \to 0$ the form factor of the spherical shell becomes $f_{\mathrm{shell}} \approx 1$, so that

$$I_{\mathrm{shell}}(0) \propto V_{\mathrm{shell}}^2 \propto \left( R_{\mathrm{out}}^3 - R_{\mathrm{in}}^3 \right)^2 . \tag{3}$$

For example, if we consider an outer radius of $R_{\mathrm{out}} = 40$ nm and an inner radius $R_{\mathrm{in}} = 35$ nm in the original state, then the radii of fused spherical shells are approximately $R_{\mathrm{out}} = 50$ nm and $R_{\mathrm{in}} = 45$ nm by assuming that the volume of the two spherical shells remain after fusion, that means $V_{\mathrm{fused}} = 2V$ and thus $R_{\mathrm{fused}} = 2^{1/3}R$. This assumption yields an increase of $\sim 56\%$ of the forward scattering intensity, which is far away from the experimental observations. Altogether, the results indicate that some reactions occurred, but we can not clearly distinguish between a docked and a fused state, most likely, due to a very low efficiency of the reactions.

## Supporting References


1. Castorph, S., S. Schwarz Henriques, M. Holt, D. Riedel, R. Jahn, and T. Salditt. 2011. Synaptic vesicles studied by dynamic light scattering. *Eur. Phys. J. E.* 34:1–11.

2. Hernandez, J. M., A. Stein, E. Behrmann, D. Riedel, A. Cypionka, Z. Farsi, P. J. Walla, S. Raunser, and R. Jahn. 2004. Membrane Fusion Intermediates via Directional and Full Assembly of the SNARE Complex. *Science.* 336:1581–1584.

3. Als-Nielsen, J., and D. McMorrow. 2011. Bibliography, in Elements of Modern X-ray Physics, Second Edition. John Wiley & Sons, Inc. Hoboken, NJ, USA.